Diagnosis of a North American Polar/Subtropical Jet Superposition Employing Piecewise Potential Vorticity Inversion

By

ANDREW C. WINTERS[1*] and JONATHAN E. MARTIN[2]

[1]Department of Atmospheric and Environmental Sciences
University at Albany – State University of New York
Albany, NY 12222

[2]Department of Atmospheric and Oceanic Sciences
University of Wisconsin-Madison
Madison, WI 53706

Submitted for publication in *Monthly Weather Review*
11 July 2016

[*] *Corresponding author address:* Andrew C. Winters, Dept. of Atmospheric and Environmental Sciences, University at Albany, SUNY, 1400 Washington Ave., Albany, NY 12222. E-mail: acwinters@albany.edu

Abstract

The polar jet (PJ) and subtropical jet (STJ) often reside in different climatological latitude bands. On occasion, the meridional separation between the two jets can vanish, resulting in a relatively rare vertical superposition of the PJ and STJ. A large-scale environment conducive to jet superposition can be conceptualized as one that facilitates the simultaneous advection of tropopause-level potential vorticity (PV) perturbations along the polar and subtropical waveguides towards middle latitudes. Once these PV perturbations are transported into close proximity to one another, interactions between tropopause-level, lower-tropospheric, and diabatically-generated PV perturbations work to restructure the tropopause into the two-step, pole-to-equator tropopause structure characteristic of a jet superposition.

This study employs piecewise PV inversion to diagnose the interactions between large-scale PV perturbations throughout the development of a jet superposition during the 18–20 December 2009 Mid-Atlantic Blizzard. While the influence of PV perturbations in the lower troposphere as well as those generated via diabatic processes were notable in this case, tropopause-level PV perturbations played the most substantial role in restructuring the tropopause prior to jet superposition. A novel PV partitioning scheme is presented that isolates PV perturbations associated with the PJ and STJ, respectively. Inversion of the jet-specific PV perturbations suggests that these separate features make distinct contributions to the restructuring of the tropopause that characterizes the development of a jet superposition.

1. Introduction

The atmosphere typically exhibits the three-step pole-to-equator tropopause structure shown in Fig. 1a, with each break in the tropopause height associated with a jet stream[1]. The polar jet (PJ) stream resides at middle latitudes in the break between the polar (~350 hPa) and subtropical (~250 hPa) tropopauses and is situated atop the strongly baroclinic, tropospheric-deep polar front (e.g., Palmén and Newton 1948; Namias and Clapp 1949; Newton 1954; Palmén and Newton 1969; Keyser and Shapiro 1986; Shapiro and Keyser 1990). The subtropical jet (STJ) stream is located equatorward of the PJ (~30°N in the Northern Hemisphere) in the break between the subtropical tropopause and the even higher tropical tropopause (~100 hPa) and is characterized by modest baroclinicity in the upper troposphere and lower stratosphere (e.g., Loewe and Radok 1950; Yeh 1950; Koteswaram 1953; Mohri 1953; Koteswaram and Parthasarathy 1954; Sutcliffe and Bannon 1954; Krishnamurti 1961; Riehl 1962).

While the separate polar and subtropical jets typically reside in different climatological latitude bands, their meridional separation occasionally vanishes, resulting in a relatively rare vertical superposition of the PJ and STJ (Christenson 2013). A vertical cross section through a jet superposition is shown in Fig. 1b, which highlights three of the primary attributes of a superposition: (1) the development of a two-step tropopause structure from polar to tropical latitudes, rather than the more common three-step structure shown in Fig. 1a, (2) a consolidation of the upper-tropospheric and lower-stratospheric baroclinicity associated with each jet into substantially narrower zones of contrast, and (3) anomalously strong wind speeds associated with the aforementioned increase in baroclinicity.

---

[1] Throughout this study, tropopause specifically refers to the dynamic tropopause, which is defined as a surface of constant potential vorticity (e.g., Morgan and Nielsen-Gammon 1998). In line with previous work, we select the 2-PVU surface (1 PVU = 10^{-6} K m^{2} kg^{-1} s^{-1}). The term, jet, will also be synonymous with jet streak in the text and refers to a zonally confined wind speed maximum along either the polar or subtropical waveguide.

The observations of the tropopause discussed with reference to Fig. 1 served as the foundation for the objective identification scheme for the PJ, STJ, and superposed jets outlined in Winters and Martin (2014). Employing that jet identification scheme as part of an analysis of the historic 1–3 May 2010 Nashville Flood, Winters and Martin (2014) determined that the development of a jet superposition was a critical component in the evolution of that flooding event. A cursory reexamination of a number of other historical and recent high-impact weather events over North America and the North Atlantic by the authors suggests that superposed jets were a component of their evolution, as well (e.g., Defant 1959; Hoskins and Berrisford 1988; Hakim et al. 1995, 1996; Bosart et al. 1996; Christenson 2013).

The association of jet superpositions with a class of high-impact weather events motivated Winters and Martin (2016, hereafter WM16) to diagnose the development of a jet superposition in two cases: the 18–20 December 2009 Mid-Atlantic Blizzard and the aforementioned 1–3 May 2010 Nashville Flood. These cases demonstrated that elements of both the antecedent remote and local synoptic environments are important to consider when diagnosing the development of a superposition. A large-scale environment conducive to jet superposition is broadly conceptualized in Fig. 2 as one that facilitates the simultaneous advection of tropopause-level cyclonic and anticyclonic potential vorticity (PV) perturbations from polar and tropical latitudes, respectively, and the subsequent horizontal juxtaposition of those PV perturbations at middle latitudes.

Much attention in the literature has focused on the origin and characteristics of these tropopause-level PV perturbations. Polar cyclonic PV perturbations, which have been referred to as coherent tropopause disturbances (CTDs; Pyle et al. 2004), are typically located along the polar waveguide, accompanied by a PJ on their equatorward flank (Fig. 2), and exhibit a localized depression in the height of the tropopause. One particular class of CTD that has received specific attention is the tropopause polar vortex (TPV), which primarily forms as a result of an enhanced vertical gradient in radiative heating near the tropopause at polar latitudes (Cavallo and Hakim 2010). As CTDs are transported towards middle latitudes by the background flow within which they are embedded, they occasionally initiate surface cyclogenesis (e.g., Hakim et al. 1995, 1996; Pyle et al. 2004; Cavallo and Hakim 2010).

In contrast to polar latitudes, where polar cyclonic PV perturbations are manifest on the tropopause as coherent vortices, tropical anticyclonic PV perturbations are not readily identifiable on the tropopause at tropical latitudes (i.e., Morgan and Nielsen-Gammon 1998, their Fig. 2). Instead, the tropical upper-troposphere is characterized by a reservoir of uniform, low PV air that is continuously replenished by mass deposition in the upper troposphere from tropical convection. Once this tropical, low PV air is transported poleward via tropical plumes or the presence of a low-latitude trough (e.g., Liebmann and Hartmann 1984; Roundy et al. 2010; Fröhlich et al. 2013; Archambault et al. 2013, 2015; WM16), it becomes manifest as an anticyclonic PV perturbation along the subtropical waveguide with a STJ positioned on its poleward flank (Fig. 2). Not only are these tropical anticyclonic PV perturbations accompanied by an upper-tropospheric thermodynamic environment characterized by weak static stability, but also by the occasional presence of atmospheric rivers (Newell et al. 1992; Zhu and Newell 1998) within the poleward-directed branch of their anticyclonic circulation. Consequently, the horizontal juxtaposition of polar cyclonic and tropical anticyclonic PV perturbations at middle latitudes typifies a dynamical and thermodynamic environment conducive to the production of high-impact weather.

As polar cyclonic and tropical anticyclonic PV perturbations are transported into close proximity to one another, the individual non-divergent circulations associated with each PV perturbation add constructively to produce the anomalously strong upper-tropospheric wind speeds associated with a superposed jet. In addition, mesoscale processes within the near-jet environment, such as ageostrophic transverse circulations and proximate midlatitude convection (Fig. 2), can act to locally restructure the tropopause into the two-step structure characteristic of a jet superposition (WM16). While WM16 note the relevance of dynamical structures within the remote synoptic environment to the production of a superposition, stronger emphasis is placed on the role of mesoscale processes within the near-jet environment. Consequently, a detailed understanding of the large-scale interaction between tropopause-level PV perturbations along the polar and subtropical waveguides during a jet superposition event remains unresolved.

A particularly effective way to examine the large-scale interaction between separate PV perturbations during the development of a jet superposition is to employ piecewise PV inversion, which leverages the intrinsic principles of PV conservation and invertibility (e.g., Hoskins et al. 1985; Thorpe 1985; Robinson 1988; Holopainen and Kaurola 1991; Davis and Emanuel 1991). Specifically, these principles imply that (1) the PV serves as a particularly good tracer for atmospheric motion under the assumption of adiabatic and inviscid flow and (2) knowledge of a PV perturbation at a particular time, along with a suitable balance condition, permits a recovery of the mass and thermal fields associated with that PV perturbation.

Piecewise PV inversion has been employed extensively to examine a number of different tropospheric processes. In particular, piecewise PV inversion has fostered insight into surface cyclogenesis (e.g., Davis and Emanuel 1991; Davis 1992; Davis et al. 1993; Davis et al. 1996; Nielsen-Gammon and Lefevre 1996; Morgan and Nielsen-Gammon 1998), midlatitude trough interaction (e.g., Hakim et al. 1996), tropospheric frontogenesis (e.g., Morgan 1999; Korner and Martin 2000), the development and movement of tropical cyclones (e.g., Wu and Emanuel 1995a,b; Shapiro 1996; Shapiro and Franklin 1999; McTaggart-Cowan et al. 2001; Shapiro and Möller 2003), and understanding of tropical–extratropical interactions (e.g., McTaggart-Cowan et al. 2001, 2004, Agustí-Panareda et al. 2004; Ahmadi-Givi et al. 2004; Grams et al. 2011, 2013).

The analysis performed by Wandishin et al. (2000), however, is of particular relevance when considering the application of PV inversion to diagnose the development of a jet superposition. In that study, piecewise quasi-geostrophic (QG) PV inversion was employed to examine the development of an idealized tropopause break. The analysis determined that vertical motion at the tropopause initiated the development of a tropopause break by vertically tilting an initially flat portion of the tropopause. Once the tropopause exhibited a vertical slope, the presence of a vertical shear acted to further tilt the tropopause in the vertical, completing the production of the tropopause break (Wandishin et al. 2000; their Fig. 4).

For the present work, which centers on diagnosing the vertical alignment of two distinct tropopause breaks, differential horizontal displacement and vertical motion are likely to play important roles. As an idealized example, Fig. 3 depicts a stronger horizontal wind component normal to the subtropical tropopause break than that normal to the polar tropopause break (red arrows). This enables a differential horizontal displacement of the two tropopause breaks that may promote their vertical alignment at a later time. In addition, vertical motion (blue arrow) positioned between the polar and subtropical tropopause breaks has the capability to alter the elevation of the subtropical tropopause and contribute to the production of the two-step tropopause structure characteristic of a jet superposition (WM16).

While the nature of the interaction between tropopause-level PV perturbations along the polar and subtropical waveguides, and their role in the production of a jet superposition, is of particular interest to this study, it is also apparent that jet superposition events can be associated with surface cyclogenesis and midlatitude convection (WM16). Consequently, a holistic understanding of the process of jet superposition from a PV perspective necessitates consideration of the influence that both lower-tropospheric and diabatically-generated PV perturbations have on the production of a jet superposition, as well. With this in mind, the forthcoming analysis isolates tropopause-level, lower-tropospheric, and diabatically-generated PV perturbations during a well-established case of jet superposition analyzed by WM16. These PV perturbations are subsequently inverted in an effort to diagnose the dynamical structures that contribute the most towards restructuring the tropopause during a jet superposition event.

The remainder of this study is structured as follows. Section 2 discusses the methodology employed in this study to partition the PV distribution and to perform piecewise PV inversion. Section 3 applies piecewise PV inversion to a well-established case of jet superposition previously examined by WM16 and Section 4 finishes with a brief discussion and some conclusions.

2. Methodology

This study considers the development of a jet superposition during the 18–20 December 2009 Mid-Atlantic Blizzard, which was chosen to complement the analysis previously performed on this case by WM16. For more specific information on the impacts of this case, the reader is referred to WM16. Wind, temperature, geopotential height, and relative humidity data for this case was acquired from National Centers for Environmental Prediction (NCEP) Global Forecast System (GFS) analyses at 6-h intervals during the 6-day period, 0000 UTC 17 December 2009 –

0000 UTC 23 December 2009. The data has a horizontal grid spacing of 1.0° × 1.0° and 20 vertical levels, with a vertical grid spacing of 50 hPa between 1000–50-hPa. This data served as boundary conditions for performing the piecewise PV inversion. The details of the inversion techniques are provided in the discussion that follows.

a) PV Partitioning Scheme

The degree to which insight is gained from piecewise PV inversion is highly dependent upon the scheme used to partition the PV distribution. Consequently, care must be taken to partition the flow into a finite number of pieces, such that each piece captures a subset of the PV distribution that is associated with a particular dynamical structure. The Perturbation PV (PPV) at 6-h intervals was defined as the instantaneous deviation of the full PV at a grid point from the 6-day Mean PV (MPV) at that same grid point. The PPV was further partitioned at each 6-h interval using a slightly modified version of the three-way partition described by Korner and Martin (2000).

A conceptual diagram illustrating this partition is shown in Fig. 4a. The Surface PV (SPV) isolates the PPV at grid points in the 950–850-hPa isobaric layer with a relative humidity < 70%, as well as all potential temperature perturbations (calculated against a 6-day mean for each grid point) on the bottom boundary of the domain. The SPV is designed to capture the impact of near-surface temperature perturbations that behave as PV perturbations along the bottom boundary of the domain (Bretherton 1966). The Interior PV (IPV) isolates the PPV at grid points in the 950–150-hPa isobaric layer with a relative humidity ≥ 70%. The IPV is designed to separate the diabatic creation and destruction of PV that accompanies latent heat release. Finally, the Upper-Tropospheric PV (UTPV) captures the PPV at grid points in the 650–100-hPa isobaric layer with a relative humidity < 70%, as well as all temperature perturbations on the top boundary of the domain. The UTPV isolates dry air of either stratospheric or upper-tropospheric origin and captures the PPV tied to dynamical structures in the middle and upper troposphere, including the PJ and STJ. Together, the SPV, IPV, and UTPV account for nearly all of the PPV within the domain, except for dry air between 800–700-hPa and nearly saturated air above 150-hPa. An examination of this residual PPV demonstrates that it is negligible and its omission does not significantly impact the analysis.

While a three-way partition of the PPV provides insight into the interaction between PV perturbations in the lower and upper troposphere and those generated via diabatic processes, it does not separate the influence of individual PV perturbations along the polar and subtropical waveguides during a jet superposition event (i.e., polar cyclonic and tropical anticyclonic PV perturbations). Consequently, an additional partitioning scheme is employed that isolates the PPV associated with the PJ and STJ, respectively. In the upper troposphere and lower stratosphere, an individual tropopause break is characterized in Fig. 4b by the horizontal juxtaposition of a positive PV perturbation on the poleward side of the tropopause break and a negative PV perturbation on the equatorward side of the tropopause break (e.g., Davies and Rossa 1998; Morgan and Nielsen-Gammon 1998; Pyle et al. 2004). The non-divergent circulations accompanying these PV perturbations subsequently combine to drive a jet that is situated parallel to its respective tropopause break. To capture these PV perturbations, the partition scheme isolates the PPV associated with each jet by considering the characteristic isentropic layers that contain the polar and subtropical tropopause breaks.

The isentropic layers used for the jet PV partition are subjective and are heavily dependent upon the case under consideration. For the 18–20 December 2009 Blizzard, the Polar Jet PV (PJPV) isolates the PPV at grid points in the 305–325-K isentropic layer with a relative humidity < 70%. The implementation of a relative humidity criterion in this partition is designed to remove the influence of proximate latent heat release when determining the flow associated with the PJ and STJ. The Subtropical Jet PV (STJPV) isolates the PPV at grid points in the 325–355-K isentropic layer with a relative humidity < 70%. An examination of potential temperature on the dynamic tropopause throughout this case demonstrates that the 325-K isentrope routinely intersected the subtropical tropopause step (Fig. 4b). Consequently, the 325-K surface served as a suitable isentrope to differentiate between the PJPV and STJPV.

While the PJPV and STJPV are not a strict partition of the UTPV, their sum closely approximates the distribution and magnitude of the UTPV (not shown). Consequently, an examination of the three-dimensional circulations associated with the PJPV and STJPV provides insight into the nature of the interaction between PV perturbations along the polar and subtropical waveguides during the development of a jet superposition.

b) Piecewise PV Inversion Techniques

Since substantial flow curvature and diabatic processes routinely characterize jet superposition events (WM16), an inversion of the Ertel PV (Ertel 1942) is more suitable for diagnosing the interaction between PV perturbations during a jet superposition event than QGPV inversion. For the present study, a static PV inversion was used to invert the Ertel PV for its associated geopotential, ϕ, and non-divergent streamfunction, ψ. The methodology for performing the inversion is identical to that described by Davis and Emanuel (1991) and the reader is encouraged to consult that work for any technical details.

Full and piecewise static PV inversions were performed within a North American domain bounded horizontally from 130°W–50°W and 10°N–65°N and vertically by the 1000-hPa and 50-hPa isobaric surfaces. For an inversion of the full PV, the analyzed geopotential height from the GFS was used to prescribe ϕ on the lateral boundaries. The boundary ψ was specified such that (1) the component of the wind from the GFS analysis perpendicular to the boundary was equivalent to the gradient of ψ along the boundary and (2) by ensuring that there was no net divergence out of the domain. Hydrostatic balance and the vertically averaged potential temperature, θ, between 1000–950 hPa (100–50 hPa) were used to determine ϕ and ψ on the bottom (top) boundary of the domain. In order to converge on a solution for ϕ and ψ, negative values of PV were changed to a small positive constant (0.01 PVU; 1 PVU = 10^{-6} K m^{2} kg^{-1} s^{-1}) and the static stability was not permitted to become negative.

The methodology for inverting the MPV is identical to the full PV, but with the ϕ, ψ, and θ fields from the GFS analysis replaced by a 6-day average of those variables, $\bar{\phi}$, $\bar{\psi}$, and $\bar{\theta}$, along the boundaries. Lateral and horizontal boundary conditions for an inversion of the full PPV, ϕ', ψ', and θ', were specified as the difference between the boundary ϕ, ψ, and θ from the full PV inversion and the MPV inversion (i.e., $\phi - \bar{\phi} = \phi'$). Lateral boundary conditions for ϕ' and ψ' were set to zero for inversions of the SPV, IPV, UTPV, PJPV, and STJPV, while θ' at the top and bottom boundaries for these inversions was specified according to the partitioning scheme discussed in Section 2a.

A static PV inversion only returns the balanced, non-divergent flow associated with each subset of the PV distribution. Given that vertical motion can also play a substantial role in restructuring the tropopause during a jet superposition event (WM16), recovery of the balanced divergent flow associated with each subset of the PV distribution was also required. This particular task was accomplished by inverting the system of prognostic balance equations described in Davis and Emanuel (1991). This technique returned the geopotential tendency, ϕ^{t}, streamfunction tendency, ψ^t, PV tendency, q^t, velocity potential, χ, and vertical motion, ω, associated with each subset of the PV distribution.

Convergence on a solution to the system of prognostic balance equations for this case required setting the lateral boundaries of ϕ^t, ψ^t, q^t, χ, and ω equal to zero, as well as the top and bottom boundaries of q^t, χ, and ω equal to zero. ϕ^t and ψ^t along the top and bottom boundaries were determined by calculating the time tendency of the hydrostatic equation and the potential temperature tendency, θ^t. The latent heating term ($d\theta/dt$) in the system of prognostic balance equations was calculated following the method employed in Emanuel et al. (1987) and Winters and Martin (2014). In order to converge consistently on a solution to the system of prognostic balance equations, smoothing of the individual forcing terms in the ω-equation was required. As for the static PV inversion, the reader is referred to Davis and Emanuel (1991) for more specific information on the system of prognostic balance equations and its inversion.

The combination of the static and prognostic PV inversion recovers the balanced three-dimensional flow associated with each subset of the PV distribution. The unbalanced portion of the flow cannot be returned via these methods and falls into a residual term, which primarily corresponds to the non-divergent component of the ageostrophic wind (e.g., Davis et al. 1996). For the case considered in this study, the unbalanced portion of the flow exceeded 20 m s^{-1} in the immediate vicinity of the developing superposed jet core[2] and was aligned anti-parallel to, and was considerably weaker than, the balanced non-divergent wind (not shown). Consequently, the restructuring of the tropopause accomplished by the unbalanced portion of the flow was greatly overshadowed by that of the balanced flow at all times considered. As a result, the process of

[2] Similar to this case, Davis et al. (1996) also noted that the unbalanced winds were maximized on the anticyclonic shear side of an upper-level jet stream in their analysis of the ERICA-IOP-4 storm.

superposition, insofar as it depends on rearrangement of the tropopause, was well explained by the balanced portion of the flow.

3. Jet Superposition during the 18–20 December 2009 Mid-Atlantic Blizzard

a) Case Overview

The overview that follows mirrors that provided by WM16 and it is reproduced here because of its relevance to the present study. At 0000 UTC 19 December, a confluent flow pattern was situated over the eastern United States at 250-hPa with a PJ (dashed blue line) located[3] in northwesterly flow over the Central Plains and an STJ (red dashed line) extending from Mexico northeastward over the Gulf of Mexico (Fig. 5a). The surface cyclone responsible for producing blizzard conditions across the Mid-Atlantic States was characterized by a minimum sea-level pressure below 1000 hPa and was positioned in a favorable location for continued development beneath the left exit region of the STJ. A vertical cross section through the PJ and STJ highlights the presence of a three-step tropopause structure and demonstrates that the PJ and STJ were clearly distinct structures at this time (Fig. 1a).

During the intervening 18 h, the PJ intensified and propagated downstream into the base of an upper-level trough centered over the Great Lakes, such that the PJ axis was aligned parallel to the STJ at 1800 UTC 19 December (Fig. 5b). The STJ also intensified during this interval and shifted poleward of its previous position into the southeastern United States. A cross section through both jet structures at this time demonstrates that, while the jet axes were located in closer proximity to one another, a three-step tropopause structure persisted (Fig. 9b). Additionally, the surface cyclone deepened ~8 hPa from the prior time beneath the left exit region of the STJ, as heavy snowfall continued to impact the Mid-Atlantic States in the cyclone’s northwest quadrant.

---

[3] PJ and STJ axes shown in Fig. 5 are identical to those shown in Fig. 5 of WM16. The axes were identified in WM16 by employing the objective jet identification scheme outlined in Winters and Martin (2014).

By 1200 UTC 20 December, the axis of the PJ shifted southeastward, as the trough over the Great Lakes continued to deepen, and the STJ migrated farther poleward into the southeastern United States. The combination of these displacements resulted in a vertical superposition (yellow line) of the PJ and STJ from southern Georgia northeastward to off the coast of North Carolina (Fig. 5c). A cross section through the superposed jet at this time indicates a marked increase in jet wind speeds, intensified upper-tropospheric and lower-stratospheric baroclinicity in the vicinity of the jet core, and the development of a two-step tropopause structure (Fig. 1b). Beneath the left exit region of the superposed jet, the surface cyclone continued to deepen rapidly off the New England coast, reaching a minimum sea-level pressure below 980 hPa. The preceding discussion suggests that this case contains PV perturbations associated with the PJ and STJ, as well as PV perturbations associated with the surface cyclone and its extensive precipitation shield. Consequently, it is prudent to consider the role played by each of these PV perturbations during the process of jet superposition.

For brevity, the foregoing analysis is restricted to diagnosing the displacement of the tropopause at a single time, 1800 UTC 19 December, 18 h prior to superposition. The results from this time were found to be representative of the entire 36-h period discussed above and permit a synthesis with the previous analysis performed on this case by WM16.

b) Differential Horizontal Displacement of the Tropopause Breaks

As discussed with reference to Fig. 3, both a differential horizontal displacement of the individual tropopause breaks and a vertical displacement of the tropopause steps can result in the production of a superposed jet's two-step tropopause structure. To diagnose the three-dimensional displacement of the tropopause, PV advection (PVA) within the domain was calculated by setting all values of PV < 1.5 PVU (> 2.5 PVU) equal to 1.5 PVU (2.5 PVU). This ensures that any diagnosed areas of PVA were restricted to the immediate vicinity of the 2-PVU surface and implied a horizontal or vertical displacement of the tropopause. The subsequent analysis examines the differential horizontal displacement of the polar and subtropical tropopause breaks by calculating PVA within the 1.5–2.5-PVU channel at 300- and 200-hPa, respectively. These isobaric levels are particularly suitable for diagnosing the horizontal displacement of the tropopause since they persistently intersect the polar and subtropical tropopause breaks throughout duration of the case (Fig. 1 and Fig. 9b).

The PVA within the 1.5–2.5-PVU channel accomplished along the polar (blue line) and subtropical (red line) tropopause breaks by the balanced non-divergent ($\vec{V}_{nd} = k \times \nabla\psi$) and divergent wind ($\vec{V}_d = \nabla\chi$) at 1800 UTC 19 December is shown in Fig. 6. From this analysis, it is immediately apparent that the non-divergent wind was responsible for a large majority of the PVA diagnosed along each tropopause break. In particular, the polar tropopause break outlined a hook-shaped region of high PV at 300-hPa over the upper Midwest and was characterized by a band of negative PVA (–PVA) by the non-divergent wind from the United States/Canadian border to northern Alabama and a band of positive PVA (+PVA) from the Great Lakes to the Mid-Atlantic States (Fig. 6a). With virtually no PVA provided by the divergent wind at 300-hPa (Fig. 6c), the PVA patterns associated with the non-divergent wind implied a downstream propagation of the PV hook at 300-hPa. Importantly, the portion of the polar tropopause break that paralleled the subtropical tropopause break was not characterized by substantial +PVA at this time, indicating that horizontal advection was not contributing to any systematic lateral displacement of the polar tropopause break towards its subtropical counterpart.

At 200-hPa, the subtropical tropopause break outlined the perimeter of a low-latitude trough west of Mexico and extended northeastward across the Florida peninsula (Fig. 6b).

Localized maxima in –PVA by the non-divergent wind characterized the subtropical tropopause break off the coast of South Carolina (Fig. 6b), implying a poleward shift of the subtropical tropopause break over the Atlantic Ocean toward the polar tropopause break. Such movement of the subtropical tropopause break contributed to the production of the superposition that occurred 18 h later (Fig. 5c). Farther upstream, an intermittently continuous band of +PVA by the non-divergent wind extended along the subtropical tropopause break from the base of the low-latitude trough west of Mexico northeastward towards the Gulf Coast. While a fraction of the +PVA by the non-divergent wind (Fig. 6b) was offset by a thin strip of –PVA by the divergent wind over the Gulf of Mexico (Fig. 6d), the diagnosed PVA patterns at this time indicate that the subtropical tropopause break was likely to either remain stationary or propagate eastward in locations upstream of the Florida peninsula. Consequently, the analysis does not support a superposition of the two tropopause breaks via differential horizontal displacement in locations west of Florida.

Given that the non-divergent wind was responsible for a large fraction of the PVA diagnosed along both tropopause breaks, additional insight is found by partitioning the non-divergent wind field via the piecewise PV inversion techniques described in Section 2. The non-divergent wind and PVA associated with the MPV, UTPV, and IPV are each shown in Fig. 7. The SPV non-divergent wind had a negligible influence on the horizontal displacement of the polar and subtropical tropopause breaks during this case and is not included in the subsequent analysis. Figures 7a,b demonstrate that the MPV non-divergent wind was characterized by a confluent flow pattern that accounted for a substantial fraction of the total PVA that was diagnosed along both tropopause breaks in Fig. 6. The confluent flow pattern associated with the MPV also conforms well with the conceptual model presented in Fig. 2 and appears to be essential for positioning the polar and subtropical tropopause breaks in close proximity to one another.

The UTPV non-divergent wind was characterized by a broad cyclonic circulation that was maximized in the immediate vicinity of the PV hook at 300-hPa (Figs. 7c,d). The UTPV non-divergent wind was responsible for PVA along the polar tropopause break (Fig. 7c) that was of similar magnitude to that forced by the MPV non-divergent wind (Fig. 7a), but opposite in sign. In particular, the UTPV non-divergent wind was responsible for a strip of –PVA from northern Mississippi to the Mid-Atlantic coast that was collocated with a strip of +PVA by the MPV non-divergent wind. Consequently, the competing influence of the UTPV and MPV non-divergent wind resulted in the weak PVA that was diagnosed along the portion of the polar tropopause break that paralleled the subtropical tropopause break at this time (Fig. 6a).

While the MPV non-divergent wind (Fig. 7b) was responsible for a large fraction of +PVA diagnosed along the subtropical tropopause break west of the Florida peninsula in Fig. 6b, the MPV (Fig. 7b) and UTPV (Fig. 7d) non-divergent wind combined constructively to produce –PVA east of Florida. Specifically, the UTPV non-divergent wind was characterized by southerly flow along the East Coast that resulted in a strip of –PVA east of South Carolina. As a result, both the UTPV and MPV non-divergent wind had an influence on the diagnosed poleward displacement of the subtropical tropopause break over the Atlantic Ocean (Fig. 6b) and the tendency for subtropical tropopause break to more closely approach the polar tropopause break.

Figures 7e,f demonstrate the IPV non-divergent flow was characterized by two perturbation anticyclones, with one located well off the New England coast and another situated over the Gulf of Mexico. The perturbation anticyclone off the New England coast was a direct product of the diabatic erosion of upper-tropospheric PV that accompanied the developing surface cyclone and its extensive precipitation shield (Fig. 5). However, it is apparent at this time that this perturbation anticyclone was positioned too far downstream to have an influence on the lateral displacement of the polar and subtropical tropopause breaks over the southeastern United States. In contrast, the perturbation anticyclone over the Gulf of Mexico was more favorably located to displace the subtropical tropopause break (Fig. 7f) and was associated with the outflow from persistent tropical convection downstream of the low-latitude trough (WM16; their Figs. 6,8). Despite its favorable location, however, the weak –PVA by the IPV non-divergent wind along the subtropical tropopause break over Mexico (Fig. 7f) was strongly outweighed by the +PVA accomplished by the MPV non-divergent wind (Fig. 7b).

The substantial influence of the UTPV non-divergent wind on the horizontal displacement of the tropopause breaks at this time motivates an examination of the non-divergent wind associated with the PJPV and STJPV. Recall that the PJPV and STJPV are not a strict partition of the UTPV, but closely approximate its distribution. The PJPV non-divergent wind was characterized by a perturbation cyclone that was centered squarely on the PV hook at 300-hPa (Fig. 8a). Furthermore, the non-divergent wind associated with the PJPV was maximized on the southernmost edge of the PV hook at this time, coincident with the location of the PJ axis in Fig. 5b. Figure 8a demonstrates that the PJPV non-divergent wind contributed substantially to PVA along the polar tropopause break as well, with PVA of the same sign and in the same locations as shown in Fig. 7c. The strength of the PJPV non-divergent wind was markedly weaker at 200-hPa, however, due to the strong static stability residing above the isentropic layer used to isolate the PJPV (Fig. 4b). Consequently, the PJPV non-divergent wind only accounted for weak –PVA along the subtropical tropopause break off the coast of South Carolina (Fig. 8b).

The STJPV non-divergent wind was maximized in the vicinity of the STJ axis along the subtropical tropopause break (Figs. 8c,d) and bore a great deal of qualitative similarity to the UTPV's non-divergent wind pattern (Figs. 7c,d). At 300-hPa, the STJPV non-divergent wind was associated with PVA patterns along the polar tropopause break (Fig. 8c) that were nearly identical to those associated with the PJPV (Fig. 8a), which suggests that both the PJPV and STJPV non-divergent wind had a comparable influence on the diagnosed lateral displacement of the polar tropopause break by the UTPV non-divergent wind. However, Fig. 8d shows that the STJPV non-divergent wind accounted for nearly all of the PVA diagnosed along the subtropical tropopause break in Fig. 7d. As a result, it appears that the non-divergent circulation associated with the STJPV had a greater ability to laterally displace *both* the polar and subtropical tropopause breaks.

c) Vertical Displacement of the Tropopause Breaks

Overall, the analysis at this time suggests that jet superposition via differential horizontal displacement of the two tropopause breaks was only possible off the coast of South Carolina. Recall from Fig. 5c, however, that the two jets became superposed as far west as southern Georgia at 1200 UTC 20 December. Consequently, the analysis must also consider the vertical displacement of the tropopause accomplished by the balanced vertical motion field. The balanced vertical motion field at 1800 UTC 19 December was characterized by a strip of subsidence at 400-hPa that was positioned squarely between the polar and subtropical tropopause breaks (Fig. 9a). Furthermore, a vertical cross section through both tropopause breaks indicates that the subsidence was positioned directly on and beneath the subtropical tropopause step and polar tropopause break (Fig. 9b). This subsidence was responsible for a band of +PVA along the tropopause that favored a downward displacement of the tropopause and an erosion of the subtropical tropopause step, both of which would be conducive to jet superposition.

As for the non-divergent wind, the vertical motion can be partitioned by employing a piecewise inversion of the prognostic balance equations. While the MPV non-divergent wind had a substantial influence on horizontally displacing the polar and subtropical tropopause breaks, Fig. 10a indicates that the MPV only accounted for a small fraction of the subsidence diagnosed between the two tropopause breaks. In contrast, the UTPV was associated with a continuous band of subsidence that extended along the polar tropopause break from Kansas to the East Coast (Fig. 10b), most of which was attributable to the PJPV (Fig. 10e) rather than the STJPV (Fig. 10f). The IPV (Fig. 10c) and SPV (Fig. 10d) were also associated with substantial subsidence between the two tropopause breaks, with most of the subsidence confined to the southeastern United States and in the immediate vicinity of the surface cyclone. Consequently, the analysis suggests that PV perturbations associated with the PJ, the surface cyclone, and the surface cyclone's precipitation shield were most responsible for the production of subsidence that would favor jet superposition.

WM16 demonstrated a large fraction of the subsidence observed between the two jet cores at this time was attributable to the ageostrophic transverse circulation associated with the double jet structure (their Figs. 10c,d). An advantage afforded by the piecewise PV inversion techniques employed in this study is the ability to partition the ageostrophic transverse circulation diagnosed by WM16 and to identify the dynamical structures most responsible for its production. The ageostrophic transverse circulation can be partitioned using the piecewise form of the Sawyer–Eliassen circulation equation (Sawyer 1956; Eliassen 1962) proposed by Morgan (1999):

$$\left(\gamma\frac{\partial\theta}{\partial p}\right)\frac{\partial^2\psi_{se}}{\partial y^2}+\left(2\frac{\partial M}{\partial p}\right)\frac{\partial^2\psi_{se}}{\partial y\partial p}+\left(-\frac{\partial M}{\partial y}\right)\frac{\partial^2\psi_{se}}{\partial p^2}=2\gamma\left(\frac{\partial U_g'}{\partial y}\frac{\partial\theta}{\partial x}+\frac{\partial V_g'}{\partial y}\frac{\partial\theta}{\partial y}\right) \quad (1)$$

where γ is a constant on isobaric surfaces [$\gamma = (R/fp_o)(p_o/p)^{c_v/c_p}$], p_o=1000 hPa, c_v=718 J kg^{-1} K^{-1}, c_p=1004 J kg^{-1} K^{-1}, R is the gas constant for dry air, θ is the potential temperature, and f is the Coriolis parameter. M is defined as the absolute geostrophic momentum and U_g' and V_g' are the perturbation geostrophic wind components recovered from an inversion of a subset of the PV distribution ($\overrightarrow{V_g'} = \frac{1}{f}\ \hat{k} \times \nabla\phi'$). The ageostrophic transverse circulation lies in a vertical plane perpendicular to the jet axes and is determined by the Sawyer–Eliassen streamfunction, ψ_{se}, such that the across-jet ageostrophic wind and vertical motion are defined as $v_{ag} = -\partial\psi_{se}/\partial p$ and $\omega = dp/dt = \partial\psi_{se}/\partial y$, respectively.

The technique for partitioning the ageostrophic tranverse circulation consists of isolating the geostrophic wind associated with each subset of the PV distribution and using those components of the geostrophic wind to calculate the right hand side of (1). Solution to (1) then proceeds by using the full distribution of θ and M to calculate the coefficients on the left hand side of (1) and by employing an identical method for inversion as outlined in WM16. Given that all of the operators in (1) are linear, the ageostrophic transverse circulations associated with each subset of the PV distribution add together to produce the full ageostrophic transverse circulation forced by the total geostrophic wind. The reader is referred to Eliassen (1962) or Keyser and Shapiro (1986) for a more detailed discussion of the Sawyer–Eliassen circulation equation and to Morgan (1999) for a discussion on the piecewise form of the equation.

Figure 11a shows the ageostrophic transverse circulation within the cross section C–C’ in Fig. 5b that was calculated using the total geostrophic wind from the full PV inversion. Importantly, the circulation in Fig. 11a is nearly identical that shown in Fig. 10c of WM16, which was computed using the geostrophic wind field from the GFS analysis. The ageostrophic transverse circulation in Fig. 11a was responsible for a substantial fraction of the +PVA diagnosed along the tropopause in Fig. 9b, as the subsidence driven by the ageostrophic transverse circulation was favorably located on and beneath the subtropical tropopause step. A partition of the ageostrophic transverse circulation into the piecewise circulations forced by the MPV (Fig. 11b) and PPV (Fig. 11c) geostrophic wind demonstrates that a majority of the +PVA and subsidence in Fig. 11a was associated with the ageostrophic transverse circulation tied to the PPV.

The ageostrophic transverse circulation associated with the PPV can be further partitioned into the individual circulations forced by the UTPV, IPV, and SPV geostrophic wind. Figure 12 indicates that the largest fraction of the PPV's ageostrophic transverse circulation was forced by the UTPV geostrophic wind (Fig. 12a), with minor and negligible contributions from the transverse circulations forced by the IPV (Fig. 12b) and SPV (Fig. 12c) geostrophic wind, respectively[4]. This result aligns well with the partition of the complete vertical motion field shown in Fig. 10, which attributed the greatest amount of subsidence between the polar and subtropical tropopause breaks to the UTPV in the vicinity of the cross section, C–C'. The UTPV transverse circulation can be further divided into the ageostrophic transverse circulations associated with the PJPV (Fig. 12d) and STJPV (Fig. 12e). Notably, a comparison between Fig. 12d and Fig. 12e indicates that a greater fraction of the UTPV's ageostrophic transverse circulation was associated with the PJPV. Consequently, the analysis provides additional evidence indicating that the flow associated with the PJPV had a greater ability to vertically restructure the tropopause than the flow associated with the STJPV.

[4] Vertical cross sections taken further downstream at this time show much more substantial contributions from the ageostrophic transverse circulations associated with the IPV and SPV, consistent with the analysis in Fig. 10.

4. Discussion

The preceding analysis provides additional support for the results in WM16 and for the influential role that vertical motion, and particularly ageostrophic transverse circulations, played in the production of a jet superposition during the 18–20 December 2009 Mid-Atlantic Blizzard. While a vertical displacement of the subtropical tropopause step appears to be the leading characteristic of this event, the PV analysis also suggests that a differential horizontal displacement of the polar and subtropical tropopause breaks aided in the development of a superposed jet east of the Florida peninsula. The dominant role played by vertical displacement in this case may not be representative of all superposition cases, however, as it is possible that other cases may be more strongly characterized by a differential horizontal displacement of the tropopause breaks. Consequently, a more comprehensive examination of superposition events is required to ascertain the mode through which jet superpositions develop most frequently over North America.

A novel perspective provided by this analysis was the ability to partition the flow and to attribute the development of a superposed jet to dynamical structures present throughout the troposphere and lower stratosphere during the event. In particular, the MPV non-divergent wind was characterized by a large-scale, confluent flow pattern over the eastern United States that aligned well with the conceptual model presented in Fig. 2. This confluent flow pattern was essential in transporting PV perturbations along both the polar and subtropical waveguides towards middle latitudes where they could interact with one another to restructure the tropopause and produce a superposition. Additional work is underway to examine whether the presence of a large-scale, confluent flow pattern is a common element of jet superposition events over North America and to evaluate the variability in upstream flow patterns that are conducive to jet superpositions. The ability to identify large-scale flow patterns that favor the development of jet superposition events could aid in identifying particular forecast periods that present an increased likelihood for jet superpositions and, consequently, for the development of high-impact weather.

Aside from the role played by the MPV non-divergent wind, the three-dimensional circulation associated with the UTPV accounted for the largest fraction of the PVA diagnosed along the tropopause at 1800 UTC 19 December. This result implies that PV perturbations along the polar and subtropical waveguides had the greatest influence on restructuring the tropopause during the event. While the IPV and SPV non-divergent wind did not impact the horizontal displacement of the tropopause breaks, the IPV and SPV contributed to the subsidence diagnosed between the two tropopause breaks. Consequently, the surface cyclone off the East Coast, and its associated diabatic heating, played a less substantial, though important role in the development of the superposition.

It is possible, however, that the SPV and IPV may play a larger role in restructuring the tropopause during superposition cases with more intense cyclogenesis and proximate latent heat release. Furthermore, the influence of the divergent wind was found to be minimal during the 18–20 December 2009 Blizzard. However, WM16 demonstrated that cases with extensive midlatitude convection in the vicinity of a double jet structure, such as the 1–3 May 2010 Nashville Flood, can be characterized by much stronger horizontal displacement of the tropopause by the upper-tropospheric divergent wind. Consequently, a greater sampling of jet superposition events is required to describe the characteristic types of interactions between PV perturbations during jet superposition events.

The substantial role played by the three-dimensional circulation associated with the UTPV in this case motivated isolating the influence of PV perturbations along the polar and subtropical waveguides. Interestingly, the analysis demonstrated that the STJPV non-divergent wind had a stronger ability to *horizontally* restructure the tropopause than the PJPV non-divergent wind. Physically, the PJPV non-divergent wind was limited in its ability to displace the subtropical tropopause break because of the strong static stability residing above the isentropic layer used to isolate PV perturbations along the polar waveguide (Fig. 4). Consequently, the penetration depth of the PJPV's non-divergent circulation above the polar tropopause break was extremely shallow. In contrast, the STJPV's non-divergent circulation was characterized by a deeper penetration depth below the isentropic layer used to isolate PV perturbations along the subtropical waveguide, given the weaker static stability of the upper troposphere. This contrast in the vertical extent of the non-divergent circulations associated with the PJPV and STJPV permitted the STJPV non-divergent wind to have a stronger influence on horizontally displacing both tropopause breaks.

An examination of the vertical motion associated with the PJPV and STJPV indicated that the three-dimensional circulation associated with the PJPV had a stronger ability to *vertically* restructure the tropopause. Some insight into the difference between the vertical motion field associated with the PJPV and STJPV is found by considering the forcing terms on the right hand side of the Sawyer–Eliassen circulation equation. Given that stronger baroclinicity typically resides beneath the PJ, the PJPV geostrophic wind is maximized in the immediate vicinity of the strongest tropospheric baroclinicity, by definition. In contrast, the STJPV's horizontal geostrophic circulation has to penetrate downward and laterally before it can interact with the strongest baroclinicity. Consequently, the PJPV geostrophic wind forces a stronger response from the Sawyer–Eliassen circulation equation than the STJPV geostrophic wind and correspondingly more intense subsidence beneath the subtropical tropopause step. The results from this case imply broadly that PV perturbations along the polar and subtropical waveguides may have distinctly different roles with respect to their ability to restructure the tropopause. However, additional evidence is required to verify this claim.

Finally, the techniques employed within this study offer a novel perspective from which to examine a number of different tropospheric phenomena. For example, the jet PV partition can be employed to further corroborate the results of Martius et al. (2010), who found that wave activity can be transferred from one waveguide to another, and to more broadly examine the nature of the interaction between the polar and subtropical waveguides. The jet PV partition also holds promise in its ability to interrogate a number of different phenomena that may occur within an environment characterized by multiple jet structures, such as surface cyclogenesis and extratropical transition. Lastly, the piecewise inversion of the Sawyer–Eliassen circulation equation employed in this study has potential to provide richer detail into the nature of transverse frontal circulations.

Acknowledgments

This work was funded by the National Science Foundation as part of the first author's dissertation research under the grant, AGS-1265182.

References

Agusti-Panareda, A., C. D. Thorncroft, G. C. Craig, and S. L. Gray, 2004: The extratropical transition of Hurricane Irene (1999): A potential-vorticity perspective. *Quart. J. Roy. Meteor. Soc.*, **130,** 1047–1074.

Ahmadi-Givi, F., G. C. Graig, and R. S. Plant, 2004: The dynamics of a midlatitude cyclone with very strong latent-heat release. *Quart. J. Roy. Meteor. Soc.*, **130,** 295–323.

Archambault, H. M., L. F. Bosart, D. Keyser, and J. M. Cordeira, 2013: A climatological analysis of the extratropical flow response to recurving western North Pacific tropical cyclones. *Mon. Wea. Rev.,* **141,** 2325–2346.

———, D. Keyser, L. F. Bosart, C. A. Davis, and J. M. Cordeira, 2015: A composite perspective of the extratropical flow response to recurving western North Pacific tropical cyclones. *Mon. Wea. Rev.*, **143,** 1122–1141.

Bosart, L. F., G. J. Hakim, K. R. Tyle, M. A. Bedrick, W. E. Bracken, M. J. Dickinson, and D. M. Schultz, 1996: Large-scale antecedent conditions associated with the 12–14 March 1993 cyclone ("Superstorm '93") over eastern North America. *Mon. Wea. Rev.*, **124,** 1865–1891.

Bretherton, F. P., 1966: Critical layer instability in baroclinic flows. *Quart. J. Roy. Meteor. Soc.*, **92,** 325–334.

Cavallo, S. M., and G. J. Hakim, 2010: Composite structure of tropopause polar cyclones. *Mon. Wea. Rev.*, **138,** 3840–3857.

Christenson, C. E., 2013: A synoptic-climatology of northern hemisphere polar and subtropical jet superposition events. M.S. thesis, Department of Atmospheric and Oceanic Sciences, University of Wisconsin–Madison, 62 pp.

Davies, H. C., and A. M. Rossa, 1998: PV frontogenesis and upper-tropospheric fronts. *Mon. Wea. Rev.*, **126,** 1528–1539.

Davis, C. A., and K. E. Emanuel, 1991: Potential vorticity diagnostics of cyclogenesis. *Mon. Wea. Rev.*, **119,** 1929–1953.

———, 1992: A potential vorticity diagnosis of the importance of initial structure and condensational heating in observed cyclogenesis. *Mon. Wea. Rev.*, **120,** 2409–2428.

———, M. T. Stoelinga, and Y.-H. Kuo, 1993: The integrated effect of condensation in numerical simulations of extratropical cyclogenesis. *Mon. Wea. Rev.*, **121,** 2309–2330.

———, E. D. Grell, and M. A. Shapiro, 1996: The balanced dynamical nature of a rapidly intensifying oceanic cyclone. *Mon. Wea. Rev.*, **124,** 3–26.

Defant, F., 1959: On hydrodynamic instability caused by an approach of subtropical and polarfront jet stream in northern latitudes before the onset of strong cyclogenesis. *The Atmosphere and Sea in Motion,* New York, Rockefeller and Oxford University Presses, 305–325.

Eliassen, A., 1962: On the vertical circulation in frontal zones. *Geophys. Publ.*, **24,** 147–160.

Emanuel, K. A., M. Fantini, and A. J. Thorpe, 1987: Baroclinic instability in an environment of small stability to slantwise moist convection. Part I: Two-dimensional models. *J. Atmos. Sci.*, **44,** 1559–1573.

Ertel, H., 1942: Ein neuer hydrodynamischer wirbelsatz. *Meteor. Z.*, **59,** 271–281.

Fröhlich, L., P. Knippertz, A. H. Fink, and E. Hohberger, 2013: An objective climatology of tropical plumes. *J. Climate*, **26,** 5044–5060.

Grams, C. M., H. Wernli, M. Böttcher, J. Čampa, U. Corsmeier, S. C. Jones, J. H. Keller, C.-J. Lenz, and L. Wiegand, 2011: The key role of diabatic processes in modifying the upper-tropospheric wave guide: A North Atlantic case-study. *Quart. J. Roy. Meteor. Soc.*, **137,** 2174–2193.

———, S. C. Jones, C. A. Davis, P. A. Harr, and M. Weissmann, 2013: The impact of Typhoon Jangmi (2008) on the midlatitude flow. Part I: Upper-level ridgebuilding and modification of the jet. *Quart. J. Roy. Meteor. Soc.,* **139,** 2148–2164.

Hakim, G. J., L. F. Bosart, and D. Keyser, 1995: The Ohio Valley wave-merger cyclogenesis event of 25–26 January 1978. Part I: Multiscale case study. *Mon. Wea. Rev.,* **123,** 2663–2692.

———, D. Keyser, and L. F. Bosart, 1996: The Ohio Valley wave merger cyclogenesis event of 25–26 January 1978. Part II: Diagnosis using quasigeostrophic potential vorticity inversion. *Mon. Wea. Rev.*, **124,** 2176–2205.

Holopainen, E. O., and J. Kaurola, 1991: Decomposing the atmospheric flow using potential vorticity framework. *J. Atmos. Sci.*, **48,** 2614–2625.

Hoskins, B. J., M. E. McIntyre, and A. W. Robertson, 1985: On the use and significance of isentropic potential vorticity maps. *Quart. J. Roy. Meteor. Soc.*, **111,** 877–946.

———, and P. Berrisford, 1988: A potential vorticity perspective of the storm of 15–16 October 1987. *Weather*, **43,** 122–129.

Keyser, D., and M. A. Shapiro, 1986: A review of the structure and dynamics of upper-level frontal zones. *Mon. Wea. Rev.*, **114,** 452–499.

Korner, S. O., and J. E. Martin, 2000: Piecewise frontogenesis from a potential vorticity perspective: Methodology and a case study. *Mon. Wea. Rev.*, **128,** 1266–1288.

Koteswaram, P., 1953: An analysis of the high tropospheric wind circulation over India in winter. *Indian J. Meteor. Geophys.*, **4,** 13–21.

———, and S. Parthasarathy, 1954: The mean jet stream over Indian in the pre-monsoon and post-monsoon seasons and vertical motions associated with subtropical jet streams. *Indian J. Meteor. Geophys.*, **5,** 138–156.

Krishnamurti, T. N., 1961: The subtropical jet stream of winter. *J. Meteor.*, **18,** 172–191.

Liebmann, B., and D. L. Hartmann, 1984: An observational study of tropical–midlatitude interaction on intraseasonal time scales during winter. *J. Atmos. Sci.*, **41,** 3333–3350.

Loewe, F. and V. Radok, 1950: A meridional aerological cross section in the southwest Pacific. *J. Meteor.*, **7,** 58–65.

McTaggart-Cowan, R., J. R. Gyakum, and M. K. Yau, 2001: Sensitivity testing of extratropical transitions using potential vorticity inversions to modify initial conditions: Hurricane Earl case study. *Mon. Wea. Rev.*, **129,** 1617–1636.

———, ———, and ———, 2004: The impact of tropical remnants on extratropical cyclogenesis: Case study of Hurricanes Danielle and Earl (1998). *Mon. Wea. Rev.*, **132,** 1933–1951.

Martius, O., C. Schwiertz, and H. C. Davies, 2010: Tropopause-level waveguides. *J. Atmos. Sci.*, **67,** 866–879.

Mohri, K., 1953: On the fields of wind and temperature over Japan and adjacent waters during winter of 1950–1951. *Tellus*, **5,** 340–358.

Morgan, M. C., 1999: Using piecewise potential vorticity inversion to diagnose frontogenesis. Part I: A partitioning of the Q vector applied to diagnosing surface frontogenesis and vertical motion. *Mon. Wea. Rev.*, **127,** 2796–2821.

———, and J. W. Nielsen-Gammon, 1998: Using tropopause maps to diagnose midlatitude weather systems. *Mon. Wea. Rev.*, **126,** 241–265.

Namias, J., and P. F. Clapp, 1949: Confluence theory of the high tropospheric jet stream. *J. Meteor.*, **6,** 330–336.

Newell, R. E., N. E. Newell, Y. Zhu, and C. Scott, 1992: Tropospheric rivers? – A pilot study. *Geophys. Res. Lett.*, **19,** 2401–2404.

Newton, C. W., 1954: Frontogenesis and frontolysis as a three-dimensional process. *J. Meteor.,* **11,** 449–461.

Nielsen-Gammon, J. W., and R. J. Lefevre, 1996: Piecewise tendency diagnosis of dynamical processes governing the development of an upper-tropospheric mobile trough. *J. Atmos. Sci.*, **53,** 3120–3142.

Palmén, E., and C. W. Newton, 1948: A study of the mean wind and temperature distribution in the vicinity of the polar front in winter. *J. Meteor.*, **5,** 220–226.

———, and ———, 1969: *Atmospheric Circulation Systems: Their Structure and Physical Interpretation*. Academic Press, 603 pp.

Pyle, M. E., D. Keyser, and L. F. Bosart, 2004: A diagnostic study of jet streaks: Kinematic signatures and relationship to coherent tropopause disturbances. *Mon. Wea. Rev.*, **132,** 297–319.

Riehl, H., 1962: Jet streams of the atmosphere. Dept. of Atmospheric Science Tech. Rep. 32, Colorado State University, Fort Collins, CO, 117 pp.

Robinson, W. A., 1988: Analysis of LIMS data by potential vorticity inversion. *J. Atmos. Sci.*, **45,** 2319–2342.

Roundy, P. E., K. MacRitchie, J. Asuma, and T. Melino, 2010: Modulation of the global atmospheric circulation by combined activity in the Madden–Julian Oscillation and the El Niño/Southern Oscillation during boreal winter. *J. Climate*, **23,** 4045–4059.

Sawyer, J. S., 1956: The vertical circulation at meteorological fronts and its relation to frontogenesis. *Proc. Roy. Soc. London*, **234A,** 346–362.

Shapiro, L. J., 1996: The motion of Hurricane Gloria: A potential vorticity diagnosis. *Mon. Wea. Rev.*, **124,** 2497–2508.

———, and J. L. Franklin, 1999: Potential vorticity asymmetries and tropical cyclone motion. *Mon. Wea. Rev.*, **127,** 124–131.

———, and J. D. Möller, 2003: Influence of atmospheric asymmetries on the intensification of Hurricane Opal: Piecewise PV inversion diagnosis of a GFDL model forecast. *Mon. Wea. Rev.*, **131,** 1637–1649.

Shapiro, M. A., and D. Keyser, 1990: Fronts, jet streams, and the tropopause. *Extratropical Cyclones: The Erik Palmén Memorial Volume,* C. Newton and E. O. Holopainen, Eds., Amer. Meteor. Soc., 167–191.

Sutcliffe, R. C., and J. K. Bannon, 1954: Seasonal changes in the upper-air conditions in the Mediterranean Middle East area. *Proc. Int. Association of Meteorology*, Rome, Italy, Int. Union of Geodesy and Geophysics. 322–334.

Thorpe, A. J., 1985: Diagnosis of balanced vortex structure using potential vorticity. *J. Atmos. Sci.*, **42,** 397–406.

Wandishin, M. S., J. W. Nielsen-Gammon, and D. Keyser, 2000: A potential vorticity diagnostic approach to upper-level frontogenesis within a developing baroclinic wave. *J. Atmos. Sci.*, **57,** 3918–3938.

Winters, A. C., and J. E. Martin, 2014: The role of a polar/subtropical jet superposition in the May 2010 Nashville Flood. *Wea. Forecasting*, **29,** 954–974.

———, and ———, 2016: Synoptic and mesoscale processes supporting vertical superposition of the polar and subtropical jets in two contrasting cases. *Quart. J. Roy. Meteor. Soc.*, **142,** 1133–1149.

Wu, C.-C., and K. A. Emanuel, 1995a: Potential vorticity diagnosis of hurricane movement. Part I: A case study of Hurricane Bob (1991). *Mon. Wea. Rev.*, **123,** 69–92.

———,———, 1995b: Potential vorticity diagnosis of hurricane movement. Part II: Tropical Storm Ana (1991) and Hurricane Andrew (1992). *Mon. Wea. Rev.*, **123,** 93–109.

Yeh, T. C., 1950: The circulation of the high tropopause over China in the winter of 1945–46. *Tellus*, **2,** 173–183.

Zhu, Y., and R. E. Newell, 1998: A proposed algorithm for moisture fluxes from atmospheric rivers. *Mon. Wea. Rev.*, **126,** 725–735.

Figure Captions

FIG. 1. (a) Vertical cross section, A–A' in Fig. 5a, through separate polar and subtropical jet cores at 0000 UTC 19 December 2009, with potential temperature contoured in red every 5-K, wind speed shaded following the legend in m s^{-1}, and the 2-PVU surface contoured with the thick blue line. 'PJ' and 'STJ' identify a polar and subtropical jet core, respectively, and the individual tropopause steps are labeled accordingly. (b) As in (a), but for the vertical cross section, B–B' in Fig. 5c, through a superposed jet at 1200 UTC 20 December 2009.

FIG. 2. Conceptual diagram summarizing the development of a jet superposition. The orange arrows depict the branches of an ageostrophic transverse circulation, the green circle identifies an area of convection, and the + (–) symbol corresponds to the center of a polar cyclonic (tropical anticyclonic) PV perturbation, with the blue (red) arrow indicating the movement that particular perturbation towards middle latitudes. The purple fill pattern corresponds to isotachs, with the darker shade of purple identifying faster wind speeds. The locations of the polar jet ('PJ'), subtropical jet ('STJ'), and superposed jets are labeled accordingly. For additional information on interpretation, please refer to the discussion in the text.

FIG. 3. Conceptual diagram illustrating the two ways a three-step tropopause can be restructured into the two-step tropopause characteristic of a superposed jet. The thick black line corresponds to the 2-PVU surface within the cross section A–A' in Fig. 5a, with the gray shading identifying the stratosphere. The red arrows correspond to the horizontal displacement of an individual tropopause break and the blue arrows identify a vertical displacement of the subtropical tropopause step.

FIG. 4. (a) Conceptual schematic of the three-way partitioning scheme for the Perturbation PV overlaid on top of the cross section A–A’ in Fig. 5a. Potential temperature is contoured in red every 5-K, the 2-PVU surface is contoured with the thick black line, and the gray shading identifies the stratosphere. Each box in the cross section corresponds to a subset of the PV distribution and is drawn such that the top and bottom boundaries of the box identify the isobaric layer used to isolate that subset of the PV distribution. The relative humidity (RH) criterion also used to isolate each subset of the PV distribution is provided within each box. (b) Similar conventions as in (a) but for the jet PV partitioning scheme. The + and – symbols correspond to positive and negative PV perturbations, respectively, and the locations of the polar (‘PJ’) and subtropical (‘STJ’) jets are labeled accordingly. The blue (red) shading identifies the isentropic layer used to isolate the Polar Jet PV (Subtropical Jet PV).

FIG. 5. 250-hPa wind speed is shaded according to the legend in m s^{-1}, 250-hPa geopotential height is contoured in black every 12 dam, sea level pressure is contoured in green every 4 hPa below 1000 hPa, the location of the surface cyclone is identified with the red ‘L’, the precipitation shield associated with the surface cyclone is shaded in green, and the jet axes are identified according to the legend at (a) 0000 UTC 19 December 2009, (b) 1800 UTC 19 December 2009, and (c) 1200 UTC 20 December 2009.

FIG. 6. PV advection at 1800 UTC 19 December 2009 within the 1.5–2.5-PVU channel by the non-divergent wind is shaded following the legend in 10^{-5} PVU s^{-1} at (a) 300-hPa and (b) 200-hPa, with the non-divergent streamfunction contoured in black every 120×10^{5} m^{2} s^{-1}. PV

advection within the 1.5–2.5-PVU channel by the divergent wind is shaded as in (a,b) at (c) 300-hPa and (d) 200-hPa, with the divergent wind in excess of 5 m s^{-1} plotted with vectors. The 2-PVU surface at 300-hPa (200-hPa) is contoured in all panels with the blue (red) line and corresponds to the location of the polar (subtropical) tropopause break.

FIG. 7. PV advection at 1800 UTC 19 December 2009 within the 1.5–2.5-PVU channel by the non-divergent wind associated with the (a,b) Mean PV, (c,d) Upper-Tropospheric PV, and (e,f) Interior PV at 300-hPa and 200-hPa, respectively. Conventions are identical to those in Fig. 6, except with the streamfunction now contoured in black (negative values dashed) every 120×10^5 m^2 s^{-1} in (a,b) and every 60×10^5 m^2 s^{-1} in (c–f). The red ‘L’s (blue ‘H’s) correspond to local minima (maxima) in streamfunction.

FIG. 8. PV advection at 1800 UTC 19 December 2009 within the 1.5–2.5-PVU channel by the non-divergent wind associated with the (a,b) Polar Jet PV and (c,d) Subtropical Jet PV at 300-hPa and 200-hPa, respectively. Conventions are identical to those in Fig. 6, except with the streamfunction now contoured in black (negative values dashed) every 30×10^5 m^2 s^{-1}. The red ‘L’s (blue ‘H’s) correspond to local minima (maxima) in streamfunction.

FIG. 9. (a) 400-hPa balanced vertical motion shaded according to the legend in dPa s^{-1} at 1800 UTC 19 December 2009. The 2-PVU surface at 300-hPa (200-hPa) is contoured with the blue (red) line and corresponds to the polar (subtropical) tropopause break. (b) Vertical cross section, C–C’ in (a), with potential temperature contoured in red every 5-K, wind speeds shaded according to the legend in m s^{-1}, subsidence shaded according the legend in dPa s^{-1}, the 1.5-PVU

surface contoured with the blue line, and PV advection within the 1.5–2.5-PVU channel accomplished by the sum of the vertical motion and horizontal divergent wind fields contoured in yellow (negative values dashed) every 1×10^{-5} PVU s^{-1}.

FIG. 10. 400-hPa balanced vertical motion associated with the (a) Mean PV, (b) Upper-Tropospheric PV, (c) Interior PV, (d) Surface PV, (e) Polar Jet PV, and (f) Subtropical Jet PV at 1800 UTC 19 December 2009. Conventions are identical to those in Fig 9a.

FIG. 11. Vertical cross section, C–C' in Fig. 5c, of the Sawyer–Eliassen streamfunction at 1800 UTC 19 December 2009 associated with the (a) Full PV, (b) Mean PV, and (c) Perturbation PV, contoured in black (negative values dashed) every 300 m hPa s^{-1}, potential temperature contoured in red every 5-K, wind speed shaded according to the legend in m s^{-1}, the 1.5-PVU surface contoured in blue, subsidence associated with the Sawyer–Eliassen circulation shaded according to the legend, and PV advection within the 1.5–2.5-PVU channel by the Sawyer–Eliassen circulation contoured in yellow (negative values dashed) every 1×10^{-5} PVU s^{-1}. The arrowheads plotted on the streamfunction contours indicate the sense of the Sawyer–Eliassen circulation.

FIG. 12. Vertical cross section, C–C' in Fig. 5c, of the Sawyer–Eliassen streamfunction at 1800 UTC 19 December 2009 associated with the (a) Upper-Tropospheric PV, (b) Interior PV, (c) Surface PV, (d) Polar Jet PV, and (e) Subtropical Jet PV contoured in black (negative values dashed) every 100 m hPa s^{-1}. All other conventions are identical to those in Fig. 11.

Figures

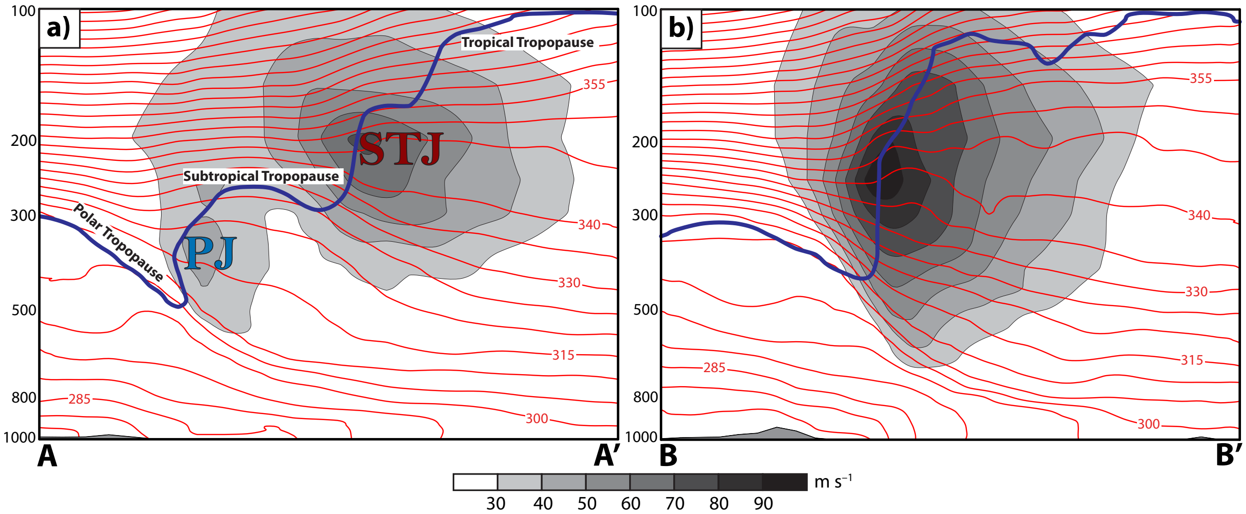

FIG. 1. (a) Vertical cross section, A–A’ in Fig. 5a, through separate polar and subtropical jet cores at 0000 UTC 19 December 2009, with potential temperature contoured in red every 5-K, wind speed shaded following the legend in m s^{-1}, and the 2-PVU surface contoured with the thick blue line. ‘PJ’ and ‘STJ’ identify a polar and subtropical jet core, respectively, and the individual tropopause steps are labeled accordingly. (b) As in (a), but for the vertical cross section, B–B’ in Fig. 5c, through a superposed jet at 1200 UTC 20 December 2009.

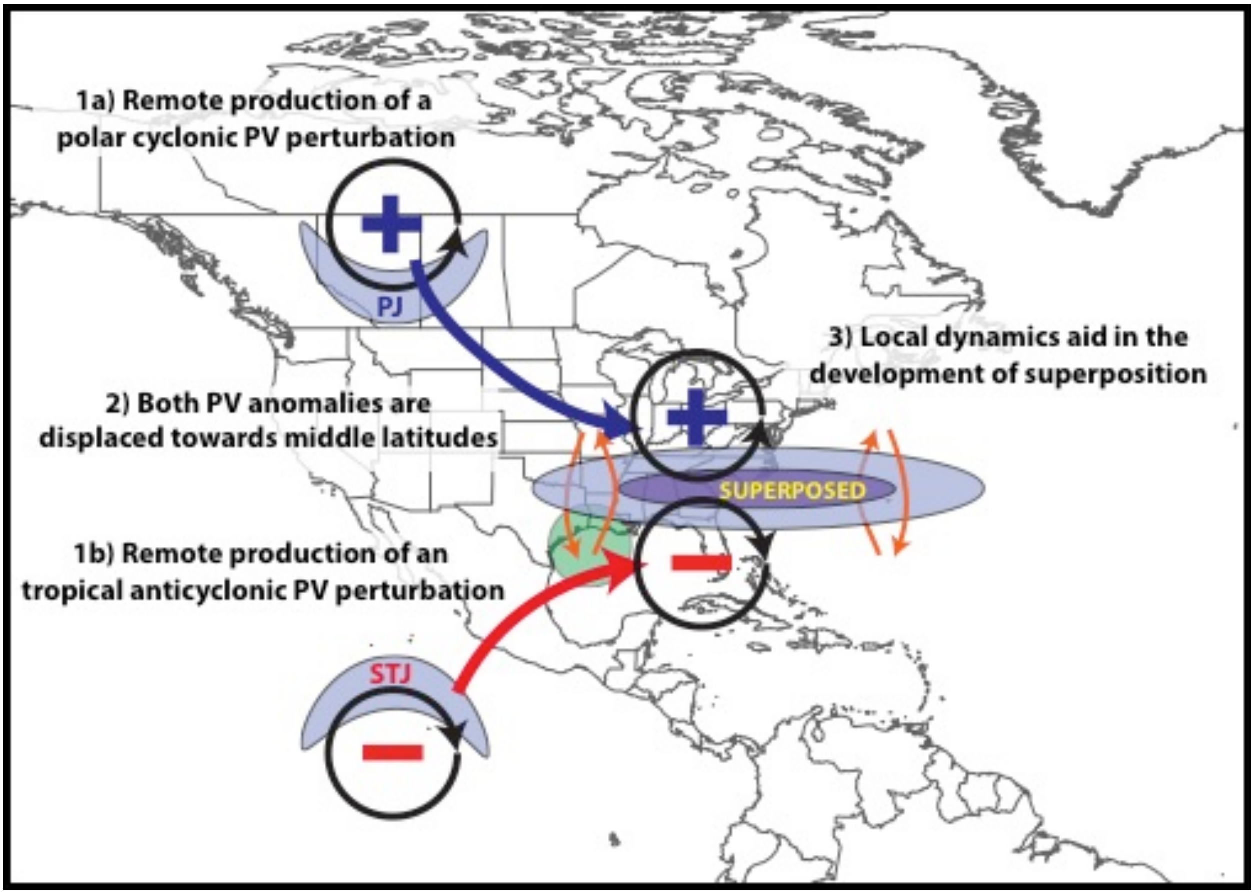

FIG. 2. Conceptual diagram summarizing the development of a jet superposition. The orange arrows depict the branches of an ageostrophic transverse circulation, the green circle identifies an area of convection, and the + (–) symbol corresponds to the center of a polar cyclonic (tropical anticyclonic) PV perturbation, with the blue (red) arrow indicating the movement that particular perturbation towards middle latitudes. The purple fill pattern corresponds to isotachs, with the darker shade of purple identifying faster wind speeds. The locations of the polar jet ('PJ'), subtropical jet ('STJ'), and superposed jets are labeled accordingly. For additional information on interpretation, please refer to the discussion in the text.

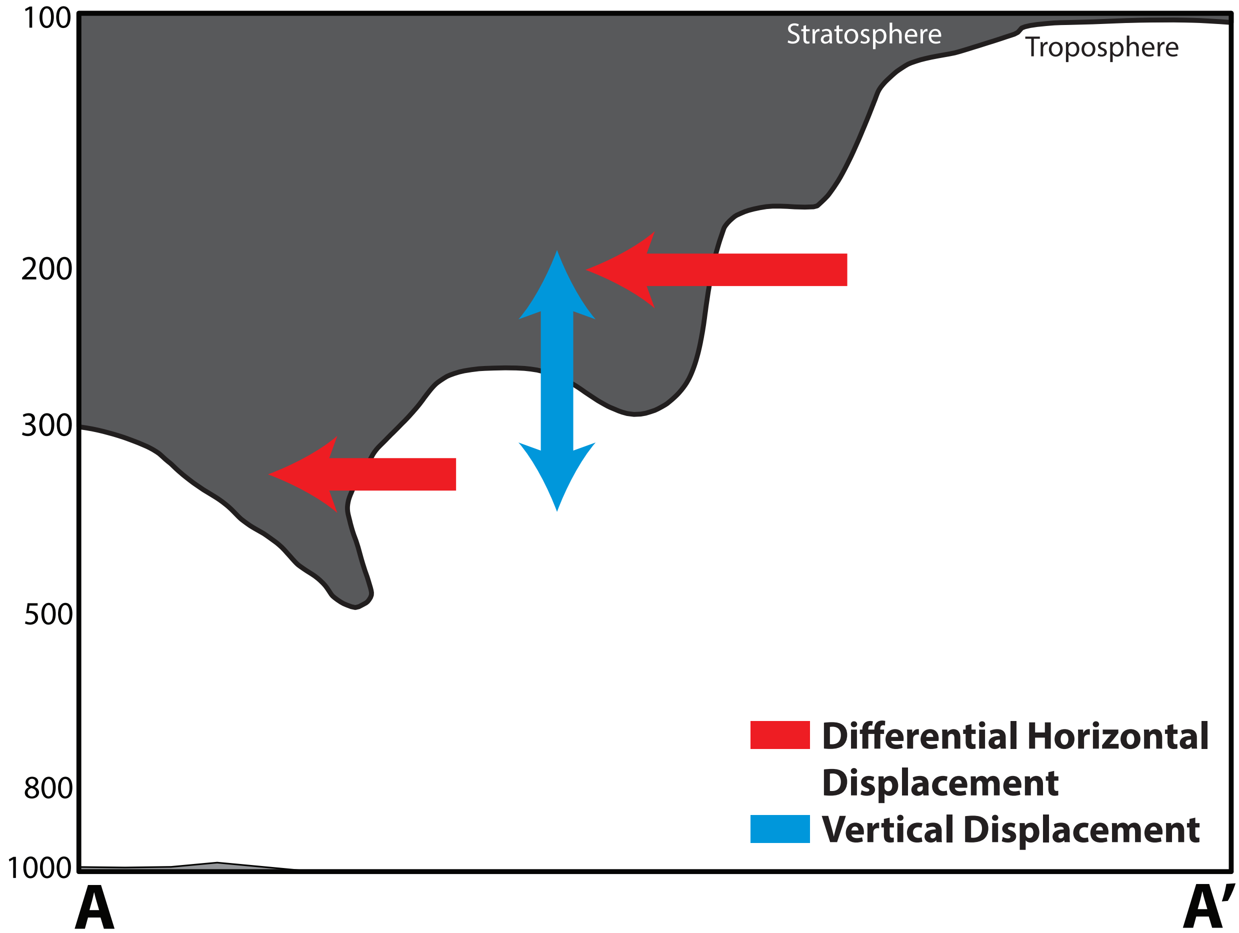

FIG. 3. Conceptual diagram illustrating the two ways a three-step tropopause can be restructured into the two-step tropopause characteristic of a superposed jet. The thick black line corresponds to the 2-PVU surface within the cross section A–A’ in Fig. 5a, with the gray shading identifying the stratosphere. The red arrows correspond to the horizontal displacement of an individual tropopause break and the blue arrows identify a vertical displacement of the subtropical tropopause step.

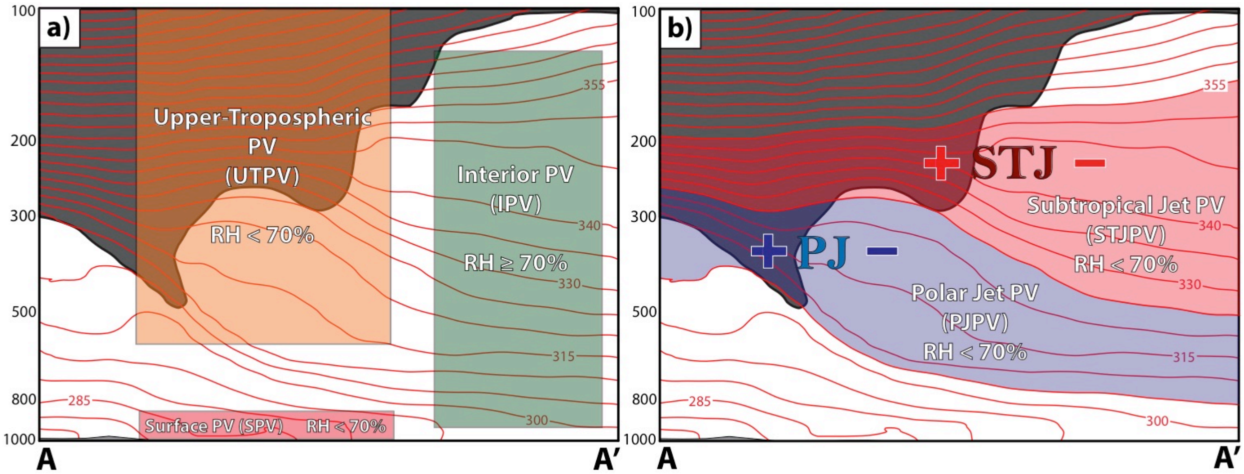

FIG. 4. (a) Conceptual schematic of the three-way partitioning scheme for the Perturbation PV overlaid on top of the cross section A–A' in Fig. 5a. Potential temperature is contoured in red every 5-K, the 2-PVU surface is contoured with the thick black line, and the gray shading identifies the stratosphere. Each box in the cross section corresponds to a subset of the PV distribution and is drawn such that the top and bottom boundaries of the box identify the isobaric layer used to isolate that subset of the PV distribution. The relative humidity (RH) criterion also used to isolate each subset of the PV distribution is provided within each box. (b) Similar conventions as in (a) but for the jet PV partitioning scheme. The + and – symbols correspond to positive and negative PV perturbations, respectively, and the locations of the polar ('PJ') and subtropical ('STJ') jets are labeled accordingly. The blue (red) shading identifies the isentropic layer used to isolate the Polar Jet PV (Subtropical Jet PV).

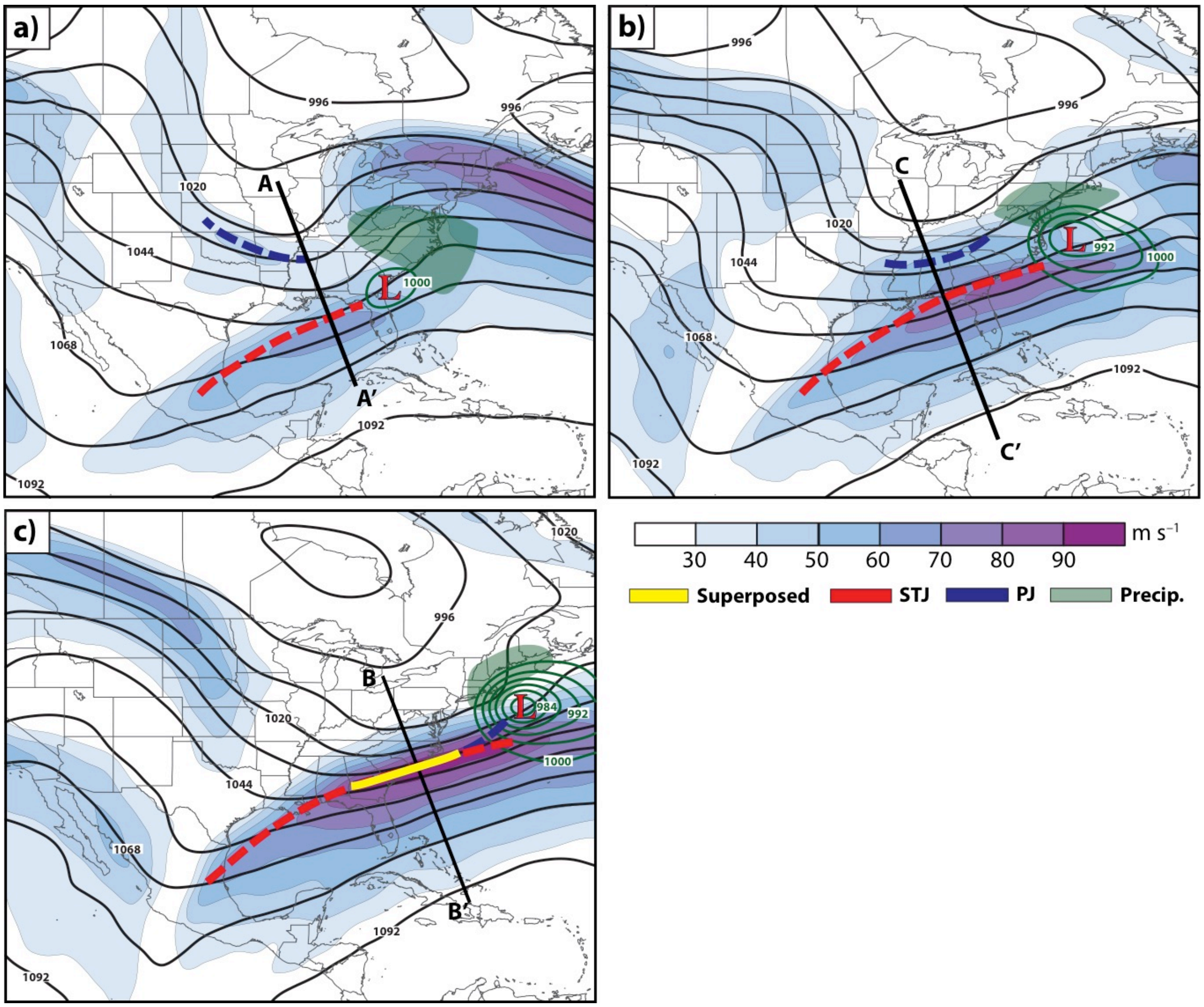

FIG. 5. 250-hPa wind speed is shaded according to the legend in m s^{-1}, 250-hPa geopotential height is contoured in black every 12 dam, sea level pressure is contoured in green every 4 hPa below 1000 hPa, the location of the surface cyclone is identified with the red ‘L’, the precipitation shield associated with the surface cyclone is shaded in green, and the jet axes are identified according to the legend at (a) 0000 UTC 19 December 2009, (b) 1800 UTC 19 December 2009, and (c) 1200 UTC 20 December 2009.

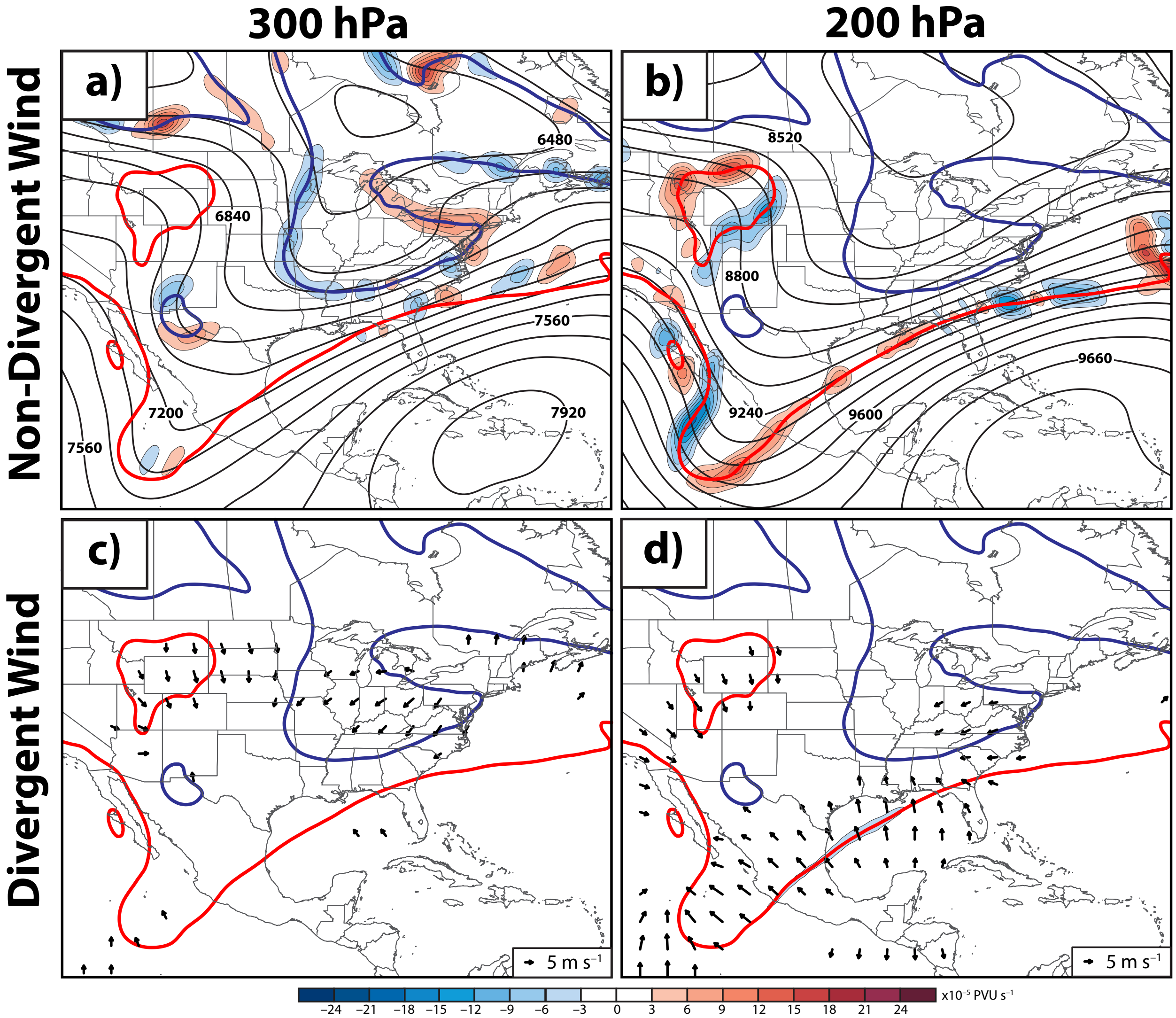

FIG. 6. PV advection at 1800 UTC 19 December 2009 within the 1.5–2.5-PVU channel by the non-divergent wind is shaded following the legend in 10^{-5} PVU s^{-1} at (a) 300-hPa and (b) 200-hPa, with the non-divergent streamfunction contoured in black every 120×10^{5} m^{2} s^{-1}. PV advection within the 1.5–2.5-PVU channel by the divergent wind is shaded as in (a,b) at (c) 300-hPa and (d) 200-hPa, with the divergent wind in excess of 5 m s^{-1} plotted with vectors. The 2-PVU surface at 300-hPa (200-hPa) is contoured in all panels with the blue (red) line and corresponds to the location of the polar (subtropical) tropopause break.

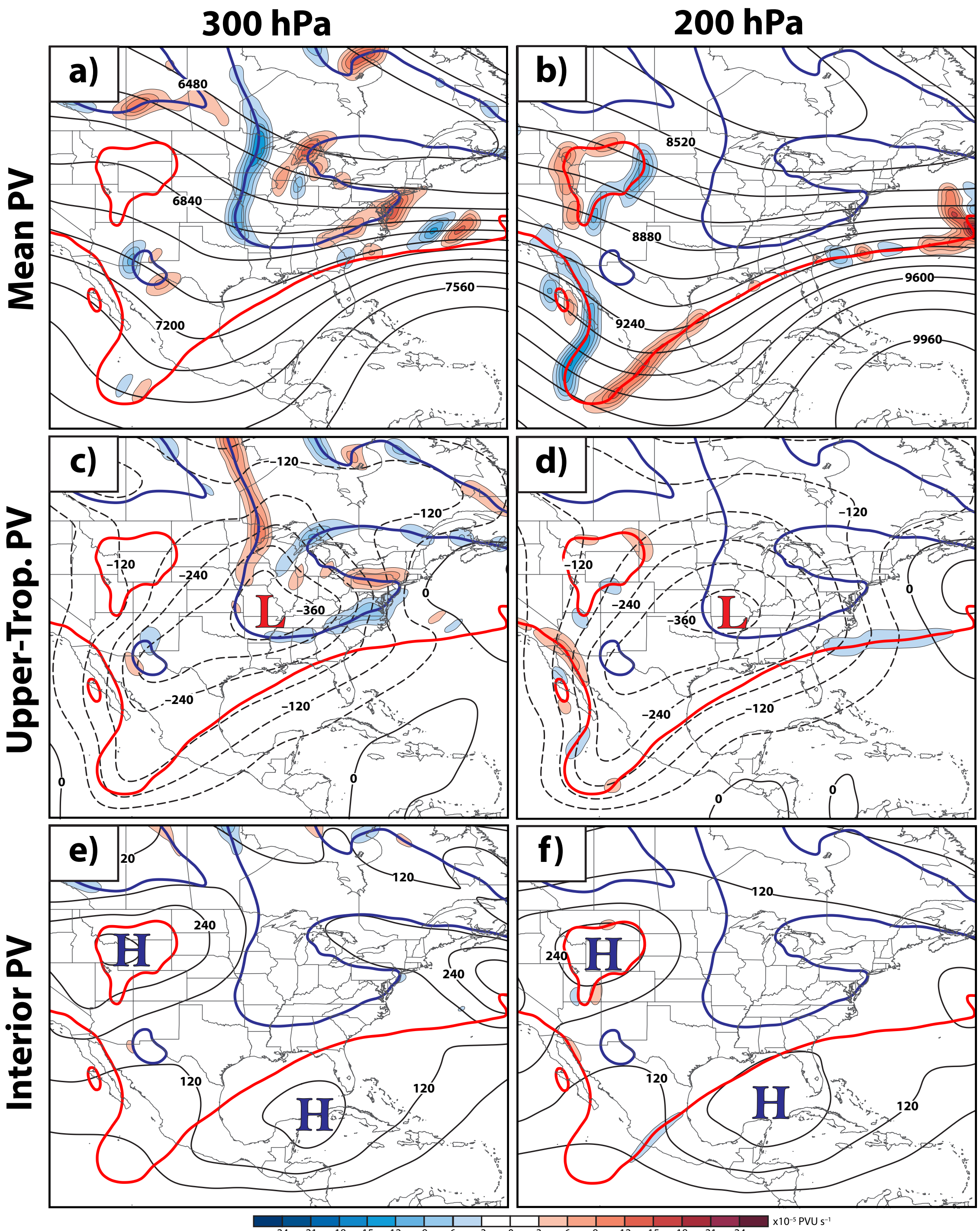

FIG. 7. PV advection at 1800 UTC 19 December 2009 within the 1.5–2.5-PVU channel by the non-divergent wind associated with the (a,b) Mean PV, (c,d) Upper-Tropospheric PV, and (e,f) Interior PV at 300-hPa and 200-hPa, respectively. Conventions are identical to those in Fig. 6, except with the streamfunction now contoured in black (negative values dashed) every 120×10^5 $m^2\ s^{-1}$ in (a,b) and every 60×10^5 $m^2\ s^{-1}$ in (c–f). The red 'L's (blue 'H's) correspond to local minima (maxima) in streamfunction.

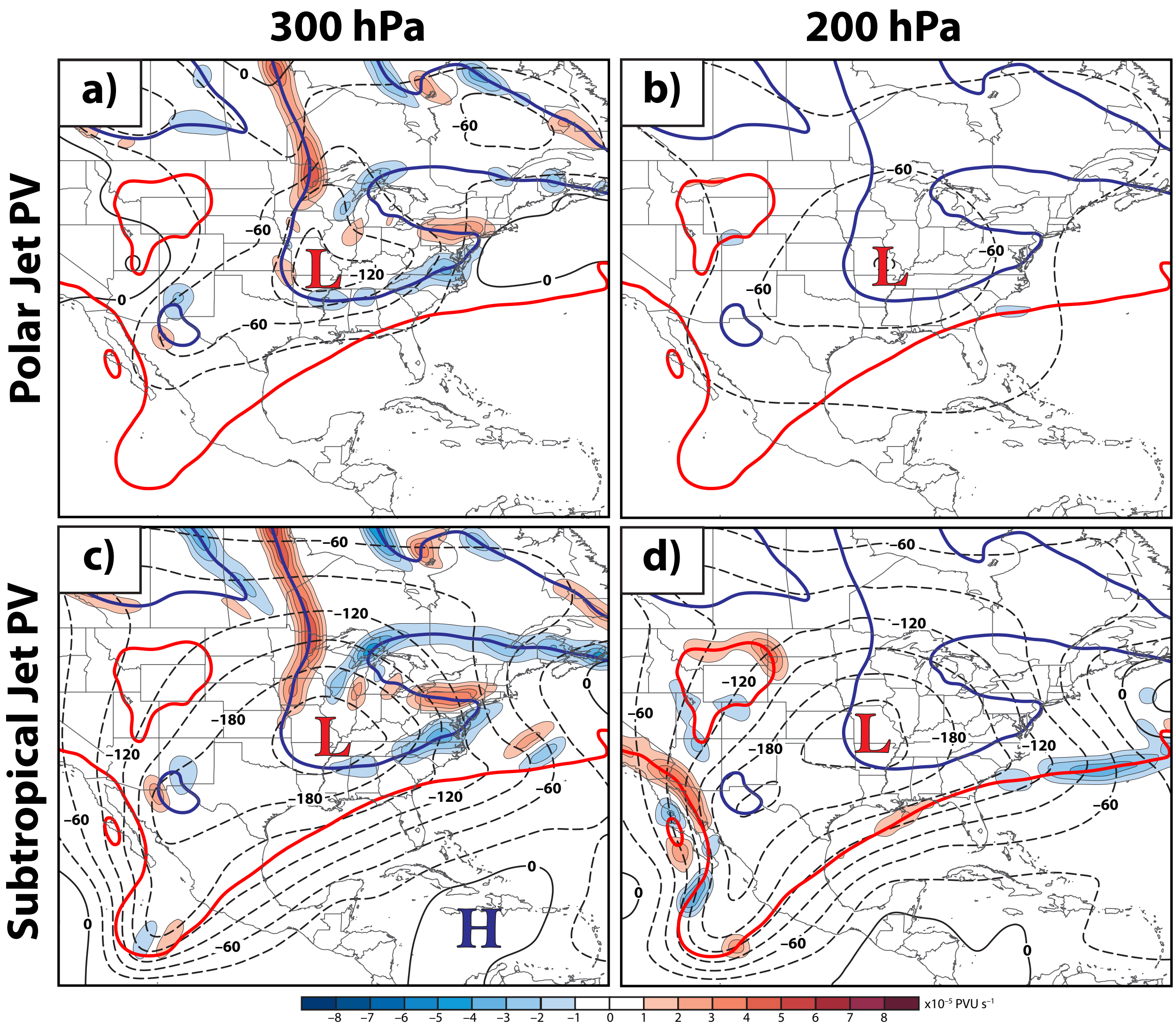

FIG. 8. PV advection at 1800 UTC 19 December 2009 within the 1.5–2.5-PVU channel by the non-divergent wind associated with the (a,b) Polar Jet PV and (c,d) Subtropical Jet PV at 300-hPa and 200-hPa, respectively. Conventions are identical to those in Fig. 6, except with the streamfunction now contoured in black (negative values dashed) every 30×10^5 m^2 s^{-1}. The red 'L's (blue 'H's) correspond to local minima (maxima) in streamfunction.

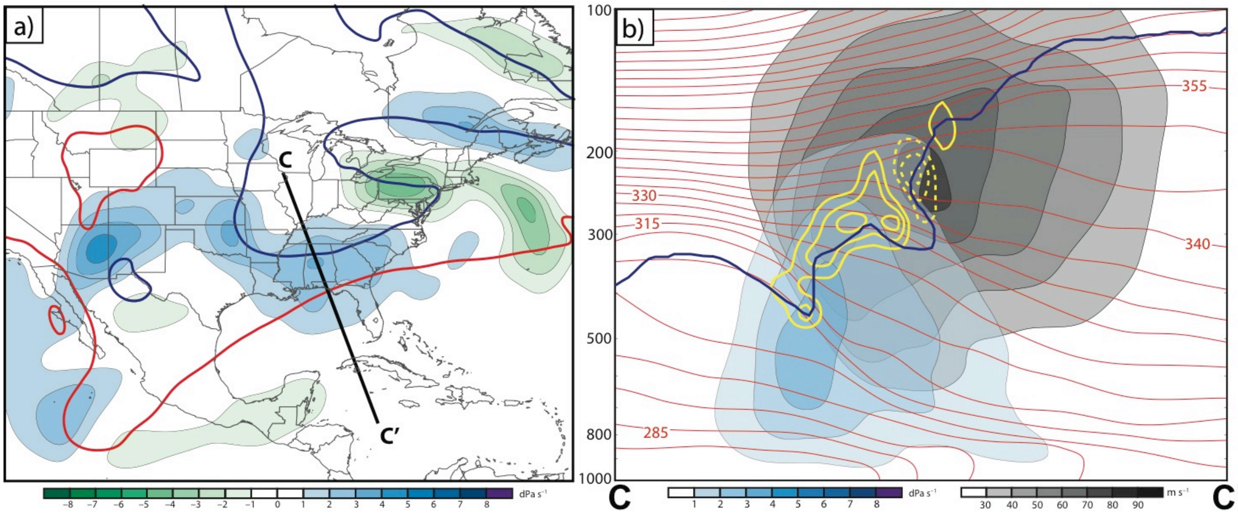

FIG. 9. (a) 400-hPa balanced vertical motion shaded according to the legend in dPa s^{-1} at 1800 UTC 19 December 2009. The 2-PVU surface at 300-hPa (200-hPa) is contoured with the blue (red) line and corresponds to the polar (subtropical) tropopause break. (b) Vertical cross section, C–C' in (a), with potential temperature contoured in red every 5-K, wind speeds shaded according to the legend in m s^{-1}, subsidence shaded according the legend in dPa s^{-1}, the 1.5-PVU surface contoured with the blue line, and PV advection within the 1.5–2.5-PVU channel accomplished by the sum of the vertical motion and horizontal divergent wind fields contoured in yellow (negative values dashed) every $1{\times}10^{-5}$ PVU s^{-1}.

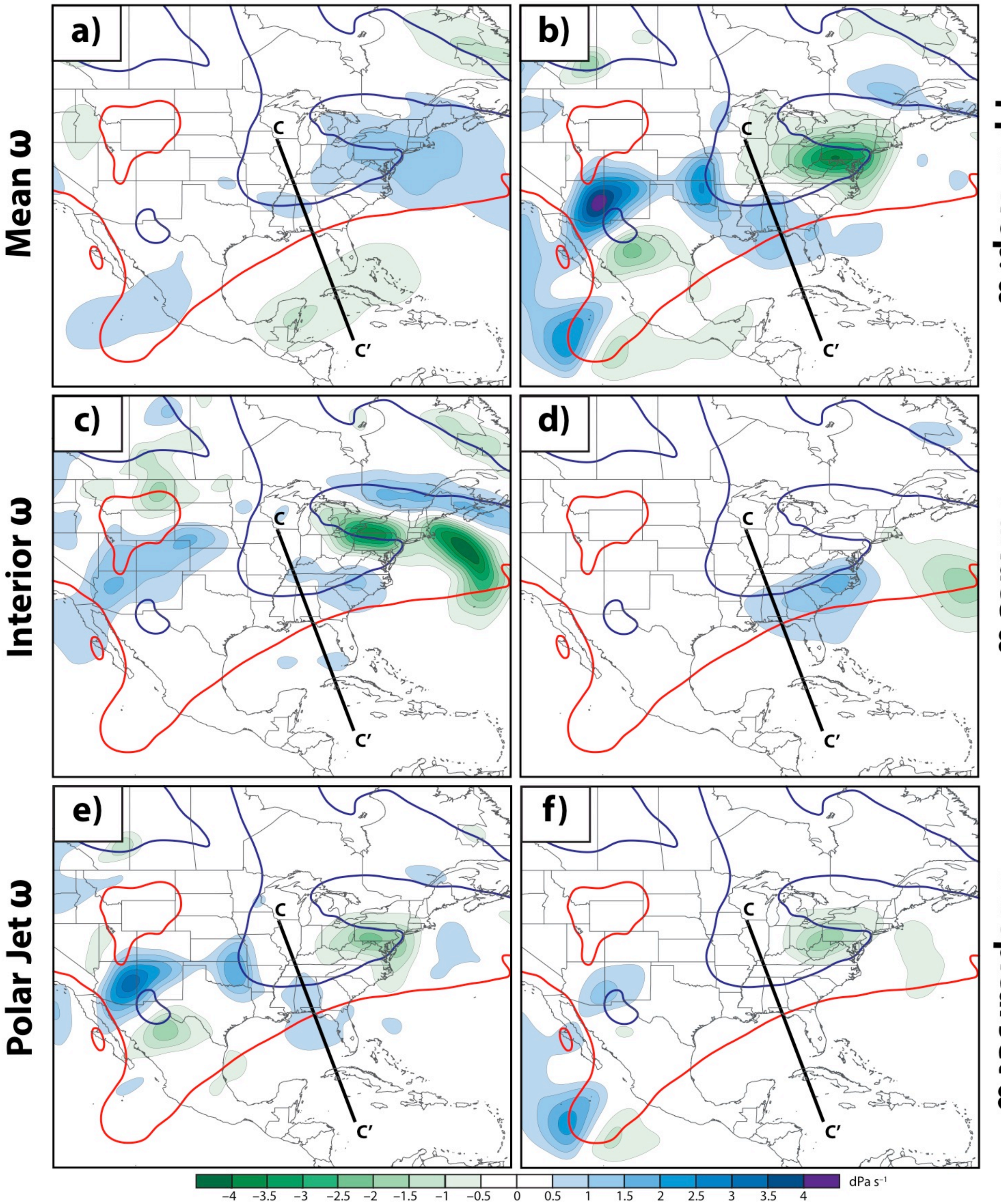

FIG. 10. 400-hPa balanced vertical motion associated with the (a) Mean PV, (b) Upper-Tropospheric PV, (c) Interior PV, (d) Surface PV, (e) Polar Jet PV, and (f) Subtropical Jet PV at 1800 UTC 19 December 2009. Conventions are identical to those in Fig 9a.

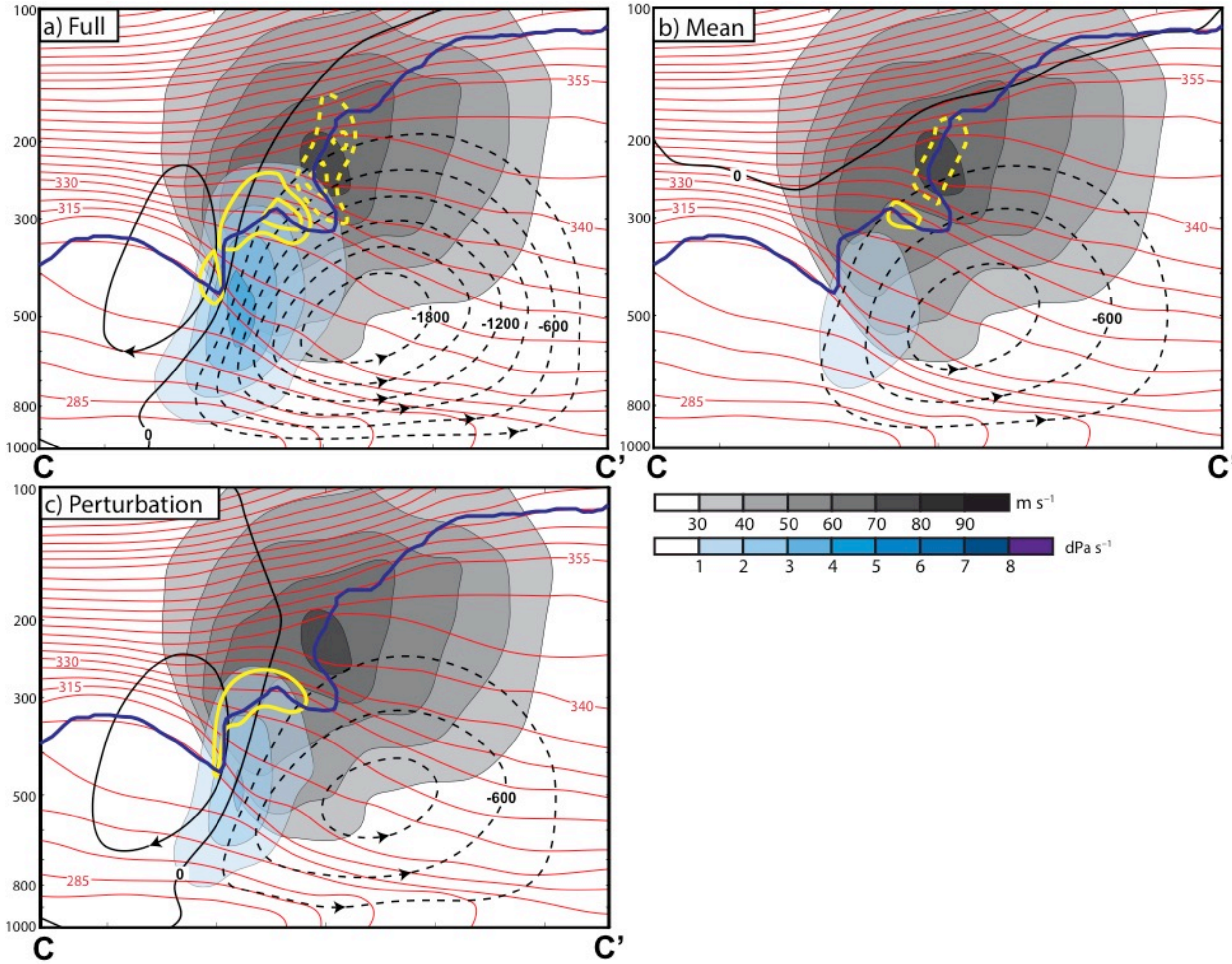

FIG. 11. Vertical cross section, C–C' in Fig. 5c, of the Sawyer–Eliassen streamfunction at 1800 UTC 19 December 2009 associated with the (a) Full PV, (b) Mean PV, and (c) Perturbation PV, contoured in black (negative values dashed) every 300 m hPa s^{-1}, potential temperature contoured in red every 5-K, wind speed shaded according to the legend in m s^{-1}, the 1.5-PVU surface contoured in blue, subsidence associated with the Sawyer–Eliassen circulation shaded according to the legend, and PV advection within the 1.5–2.5-PVU channel by the Sawyer–Eliassen circulation contoured in yellow (negative values dashed) every 1×10^{-5} PVU s^{-1}. The arrowheads plotted on the streamfunction contours indicate the sense of the Sawyer–Eliassen circulation.

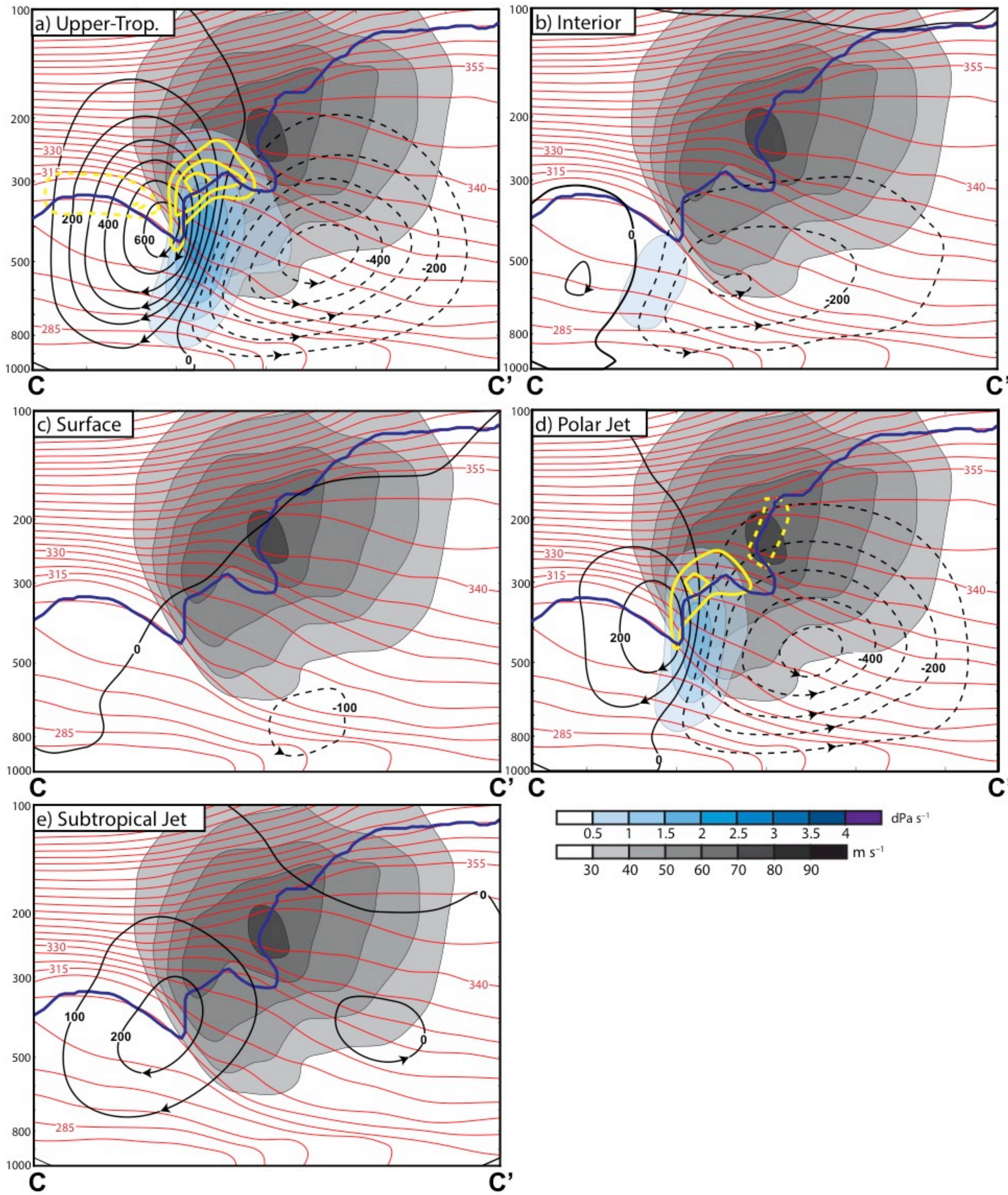

FIG. 12. Vertical cross section, C–C' in Fig. 5c, of the Sawyer–Eliassen streamfunction at 1800 UTC 19 December 2009 associated with the (a) Upper-Tropospheric PV, (b) Interior PV, (c) Surface PV, (d) Polar Jet PV, and (e) Subtropical Jet PV, contoured in black (negative values dashed) every 100 m hPa s^{-1}. All other conventions are identical to those in Fig. 11, except that PV advection is now contoured in yellow (negative values dashed) every 0.5×10^{-5} PVU s^{-1}.